Theoretical Study on Two-dimensional Crystallization of Bacteriorhodopsins Driven by Lateral Depletion Effects

須田, 慶樹

Theoretical Study on Two-dimensional Crystallization of Bacteriorhodopsins Driven by Lateral Depletion Effects

by

Keiju Suda

Department of Chemistry, Graduate School of Science, Kyushu University, Japan

ABSTRACT

Bacteriorhodopsin (bR) is a transmembrane protein. bR monomers form bR trimers, and the trimers construct a two-dimensional crystal on a bio-membrane spontaneously. The driving force for the crystallization is unclear. In this thesis, I assume the driving force as the depletion force of lipid molecules and examine the validity of the assumption. I focused on experiments conducted by M. P. Krebs et. al. They prepared mutant bRs that cannot form trimer i.e., the mutants are in monomer form. According to their research, the critical concentration (CC) for the crystallization for the bR monomer is 10.2 times higher than that for the trimer. I explain this result by using depletion force theories. To adopt the theory, the bR monomer, trimer, and lipid molecules were modeled as hard disks. The biomembrane was modeled as a two-dimensional plane space. The binary hard disk system, namely bR—lipid system, has a reservoir of lipid molecules to fix the chemical potential for lipid molecules. The phase diagrams for the bR monomer and trimer were calculated by using two theoretical approaches: two-dimensional free volume theory (2D–FVT) and thermodynamic perturbation theory with effective potential. The CCs for the monomer and the trimer were obtained from the phase diagrams. The critical concentration ratio (CCR) between the monomer and the trimer was calculated and compared with the experimental CCR.

First, the phase diagrams for the monomer and trimer were obtained by using the 2D—FVT approach. Semi-grand potentials for the fluid and ordered phases were calculated by the 2D—FVT, and pressure and chemical potential for the bR were obtained from the semi-grand potentials. The pressure and the chemical potential are the same between the fluid and ordered phases, respectively. Solving those two equations, the fluid—ordered phase coexistence region was calculated. The coexistence region for the trimer is wider than that for the monomer. That is, the bR trimers start to crystallize at the lower bR packing fraction than that for the monomer. This result agrees with the experimental one qualitatively. In addition, the CCR was obtained from the phase diagrams and showed good agreement with the experimental one. Therefore, it is indicated that the depletion force of the lipid molecules is dominant for the bR crystallization. However, I found a problem with the 2D—FVT approach that the q-dependence of the phase diagram disappears when q is very small. Therefore, the phase diagrams were also examined by another theory, namely the thermodynamic perturbation theory with effective potential.

Second, the phase diagrams for the monomer and trimer were obtained by using the thermodynamic perturbation theory (TPT) with effective potential. The AO potential and modified AO potential were adopted as the effective potential. Helmholtz free energies for the bR fluid and ordered phases were calculated by using the TPT. The phase diagrams were obtained by drawing a common tangent on the free energies. The phase diagrams obtained by adopting the AO potential as the effective potential show high CC and indicate that the depletion force is too weak to drive the bR crystallization when the repulsive core of the lipid molecules is ignored. On the other hand, the phase diagrams obtained by adopting the modified AO potential show small CC and indicate that the depletion force is enough strong to drive the crystallization when the repulsive core of the lipid molecules is considered. In addition, the CCR obtained by using the modified AO–TPT approach shows good agreement with the experimental one. Therefore, it is also indicated by the modified AO–TPT approach that the depletion force of the lipid molecules is dominant for the bR crystallization.

Contents

Chapter 1

Introduction

1.1 Phase separation caused by depletion effect

Bacteriorhodopsin (bR) is a transmembrane protein of *Halobacterium salinarum.* The bR is the light-driven proton pump, which transports the proton out of the cell. The bRs construct a two-dimensional crystal in the biomembrane [1, 2]. The crystallization is considered as essential for the bR function. For example, it is reported that the crystallization prevents the denaturation of the bR [3, 4]. The crystal contains some lipids. However the ratio, lipid weight / protein weight, in the crystal is much smaller than that in the biomembrane. That is, the crystallization can be regarded as the separation between bRs and lipids in the two-dimensional system. However, the driving force for the crystallization is unclear. For example, there is no hydrogen bond or ion bond between bRs.

I focused on the following point to consider the dominant factor for the crystallization. Most of the bR amino acid residues consist of nonpolar amino acid residues. In addition, the lipid molecule has acyl chains, which are also hydrophobic. That is, the hydrophobic interaction seems to be dominant in the biomembrane. Thus, I considered that the van der Waals picture can be adopted. According to the van der Waals picture, the liquid structure is not formed by attractive force but by repulsive force. Therefore, the bR structure seems not to be formed by direct attractive force, but by effective interaction arising from repulsive force between bRs and lipid molecules, namely depletion force. The depletion force is the effective attractive force between bRs explained by the entropy increase of lipid molecules in the canonical ensemble. I consider the hypothesis is worthwhile to study because this effective interaction is enough strong to induce crystallization in the three-dimensional hard sphere system.

1.1.1 Mixture of ideal gas model

I would like to review the research on the mixing and separation of molecules. Generally, the mixture is driven by entropy increase. The simplest model is the mixing of the ideal gas. N_1 mole ideal gas consisting of molecular species 1 and an N_2 mole ideal gas consisting of molecular species 2 are in the two insulated containers, respectively (FIG 1.1). The temperature and the pressure are the same in the two containers. The two containers are connected. When the divider is removed, the molecule 1 and the molecule 2 mix spontaneously. In an isolated system, the state changes so that the entropy increases. That is, the mixing of ideal gas is driven by the entropy increase. The difference of entropy ΔS_{mix} before and after the mixing of the gases is calculated as follows:

$$\Delta S_{\mathrm{mix}} = -\mathrm{R}(N_1 \ln[x_1] + N_2 \ln[x_2]\,, \tag{1.1}$$

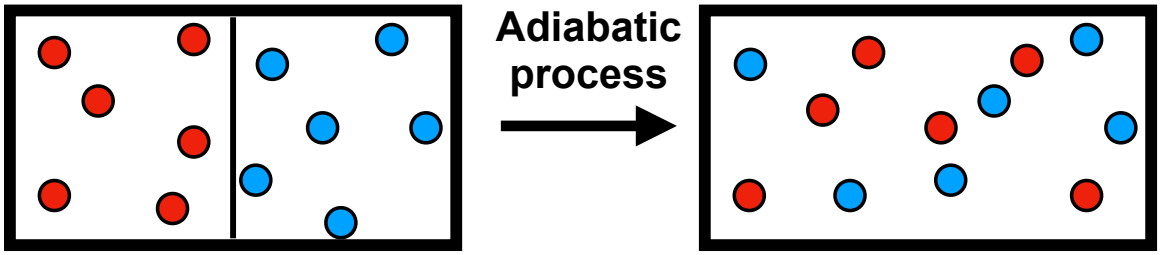

Molecule1 : N_1 mol

Molecule2 : N_2 mol

Figure 1.1: A mixture of ideal gas. Two species of molecules, molecule1 and molecule2, are in the insulated containers, respectively. When the two containers are connected, and the divider is removed, the molecules1 and molecules2 mix spontaneously.

where R is the gas constant, x_1 and x_2 are the mole fraction of the molecule 1 and molecule 2, respectively. x_1 and x_2 are written as follows:

$$x_1 = \frac{N_1}{N_1 + N_2}, \tag{1.2}$$

$$x_2 = \frac{N_2}{N_1 + N_2}. \tag{1.3}$$

Since $0 < x_1 < 1$ and $0 < x_2 < 1$, the ΔS_{mix} is positive. The eq. (1.1) shows that the entropy increases after the mixing.

1.1.2 Lattice model for mixing polymers and solvent molecules

The entropy driven mixing and energy driven demixing were shown by using a lattice model. The interactions between molecules are not considered in the ideal gas model. In 1942, Flory and Huggins independently published their theories on the mixing of polymers and solvent molecules using the lattice model [5, 6]. Their theory contains direct interactions between polymers and solvent molecules. Polymers “a” and solvent molecules “b” are mixed (FIG. 1.2). Their theory is as follows. One polymer segment and one solvent molecule occupy one lattice site. No more than two segments or solvent molecules can occupy one lattice site. A segment of the polymer is distributed next to another segment of that polymer. All lattice sites are occupied by the segments or solvent molecules. The theory assumes a random mixture of polymers and solvents. The difference of Helmholtz free energy ΔF_{mix} before and after the mixing is calculated as follows:

$$\Delta F_{\mathrm{mix}} = \Delta E_{\mathrm{mix}} - T\Delta S_{\mathrm{mix}}, \tag{1.4}$$

where ΔE_{mix} is the difference of energy before and after the mixing. ΔS_{mix} is the difference of entropy before and after the mixing. ΔS_{mix} is calculated as follows:

$$\Delta S_{\mathrm{mix}} = -\mathrm{k_B}(N_{\mathrm{a}} \ln[\phi_{\mathrm{a}}] + N_{\mathrm{b}} \ln[\phi_{\mathrm{b}}]), \tag{1.5}$$

where $\mathrm{k_B}$ is the Boltzmann constant. N_{a} and N_{b} are the number of polymers “a” and solvent molecules “b”, respectively. ϕ_{a} and ϕ_{b} are the volume fraction of polymers “a”

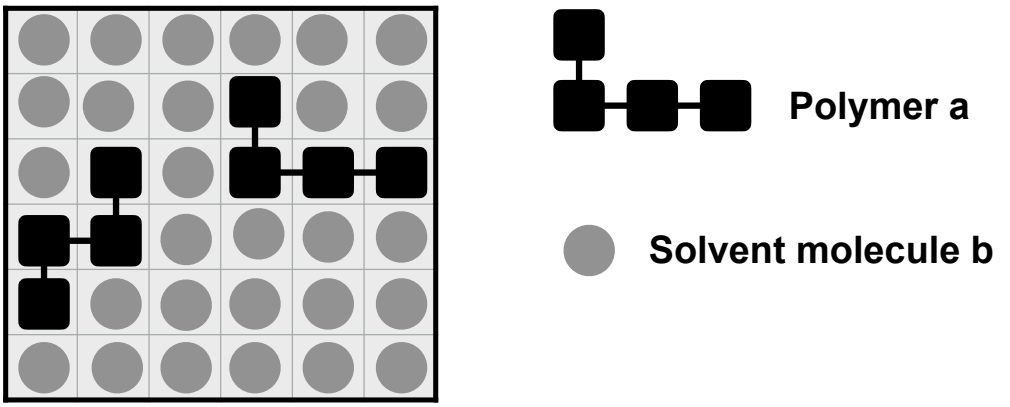

Figure 1.2: Lattice model for a mixture of polymer and solvent molecules. A square shows a segment of a polymer. A circle shows a solvent molecule.

and solvent molecules " b ", respectively. n is the number of segments in one polymer. Using the number of all lattice sites, Ω, the volume fraction is as follows:

$$\phi_{\mathrm{a}} \equiv \frac{nN_{\mathrm{a}}}{\Omega}, \tag{1.6}$$

$$\phi_{\mathrm{b}} \equiv \frac{N_{\mathrm{b}}}{\Omega}. \tag{1.7}$$

The ΔS_{mix} of the lattice model is similar to the ΔS_{mix} of the ideal gas model. However, there is a difference. ΔS_{mix} of the lattice model is calculated using the volume fraction, whereas that of the ideal gas model is calculated using the mole fraction. Since $0 < \phi_{\mathrm{a}} < 1$ and $0 < \phi_{\mathrm{b}} < 1$, the ΔS_{mix} is positive. That is, the entropy increases when the polymers and solvents are mixed. If the n segments of the polymer are decomposed so that each segment can be distributed independently, ΔS_{mix} is

$$\Delta S_{\mathrm{mix}} = -\mathrm{k_B}(nN_{\mathrm{a}}\ln[\phi_{\mathrm{a}}] + N_{\mathrm{b}}\ln[\phi_{\mathrm{b}}]). \tag{1.8}$$

This shows that ΔS_{mix} in eq. (1.8) is larger than that in eq. (1.5). That is, when the volume fraction is the same, ΔS_{mix} decreases as the number of segments in one polymer increases. The calculation of ΔE_{mix} is shown. The theory assumes that only substances in adjacent lattice sites interact with each other. The segments interact with each other by $\varepsilon_{\mathrm{AA}}$. The solvent molecules interact with each other by $\varepsilon_{\mathrm{BB}}$. The segment interacts with the solvent molecule by $\varepsilon_{\mathrm{AB}}$. ΔE_{mix} is calculated as follows:

$$\Delta E_{\mathrm{mix}} = \Omega \mathrm{k_B} T \chi \phi_{\mathrm{a}} \phi_{\mathrm{b}}, \tag{1.9}$$

where T is the temperature. χ is defined as follows:

$$\chi \equiv \frac{z\Delta\varepsilon}{\mathrm{k_B}T}, \tag{1.10}$$

$$\Delta\varepsilon \equiv \varepsilon_{\mathrm{AB}} - \frac{1}{2}(\varepsilon_{\mathrm{AA}} + \varepsilon_{\mathrm{BB}}), \tag{1.11}$$

where z is the number of nearest neighbors for one lattice site. Unlike ΔS_{mix}, ΔE_{mix} can be both positive and negative values. The eq. (1.9) shows that the sign of ΔE_{mix} depends on the sign of χ. Substituting eq. (1.5), (1.8), and (1.9) to (1.4), ΔF_{mix} is as follows:

$$\beta\Delta F_{\mathrm{mix}} = \mathrm{k_B}(N_{\mathrm{a}}\ln[\phi_{\mathrm{a}}] + N_{\mathrm{b}}\ln[\phi_{\mathrm{b}}]) + \Omega \mathrm{k_B} T \chi \phi_{\mathrm{a}} \phi_{\mathrm{b}} \tag{1.12}$$

The first term on the right-hand side is the entropy term. The entropy term is negative. On the other hand, the second term, the energy term, can be positive. For example, all interactions are attractive. In other words, ε_{AA}, ε_{BB}, and ε_{AB} are negative. When $|\varepsilon_{AA}|$ and $|\varepsilon_{BB}|$ are large and $|\varepsilon_{AB}|$ is small, χ is positive. In this case, the energy term drives the separation of polymer and solvent. That is, the Flory-Huggins theory indicates that the separation of molecules is not driven by entropy but by energy. However, various experiments in solution chemistry and other fields have shown that this conclusion is not necessarily correct. Sometimes an increase in energy due to the molecular aggregation or oligomerization is observed. Sometimes endothermic phenomena occur during association formation. The reason for this is that the lattice model ignores important factors in the real system. One of the factors is excluded volume.

1.1.3 Depletion effect

I explain excluded volume. For example, there are two hard spheres (Fig. 1.3). Two spheres diameter, R, is the same. A center of the sphere cannot approach the center of the other sphere within $2R$. The volume where the center of the other spheres cannot enter is the excluded volume. Fig. 1.3 shows that the excluded volume is larger than the volume of one sphere.

The excluded volume induces an effective attractive force between particles. For example, when the polymers are added to a colloidal solution, the colloid particles aggregate. The reason is as follows in a canonical ensemble. The centers of the polymers are excluded from the colloid particles because they are unable to overlap the colloidal particles. Therefore, the excluded volume (the dashed region in Fig. 1.4) exists around the colloid particles. When the colloid particles are in contact, the excluded volumes overlap, and the excluded volumes in the system decrease (right side in FIG. 1.4). In other words, when the colloid particles approach, the region where the centers of polymers can be distributed increases. For this reason, the number of configurations of polymers increases, and the entropy increases when the colloid particles approach. That is, the effective attractive force arises between the colloid particles because the translational entropy of the polymers increases. This is called the depletion effect. Note that in the lattice model explained in the previous section, there is no change in the excluded volume when particles come into contact with each other. That is because the volume of the particle agrees with the excluded volume. (Special lattice models exist that incorporate excluded volume effects.) Therefore, The Flory-Huggins theory [5, 6] does not contain the depletion effect.

The depletion effect was discovered by Asakura and Oosawa in the 1950s [7,8]. This effect is ignored for a long time after the discovery, but it was rediscovered by Vrij in 1976 [9]. They derived the effective potential arising from the depletion effect. This is called the Asakura—Oosawa (AO) theory [7, 8]. In the AO theory, the polymers are regarded as spheres. That is, the position of the segments within the polymer is fixed. In addition, the theory adopts an approximation that the polymers can overlap each other. The effective potential, $\omega(r)$ is calculated by the AO theory as follows:

$$\omega(r) = \infty \qquad r < 2R, \tag{1.13}$$

$$\omega(r) = -\rho k_B T \Delta V_{ex}(r) \qquad r \geq 2R, \tag{1.14}$$

where r is the distance between the centers of colloid particles, ρ is the number density of the polymers, and ΔV_{ex} is the overlapping volume of the excluded volume when the colloid particles come close.

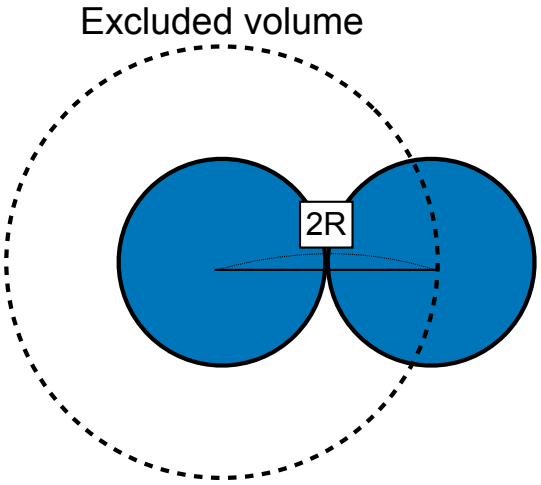

Figure 1.3: The dashed line shows the excluded volume. The center of other sphere cannot enter the dashed line. The volume surrounded by dashed line is the excluded volume.

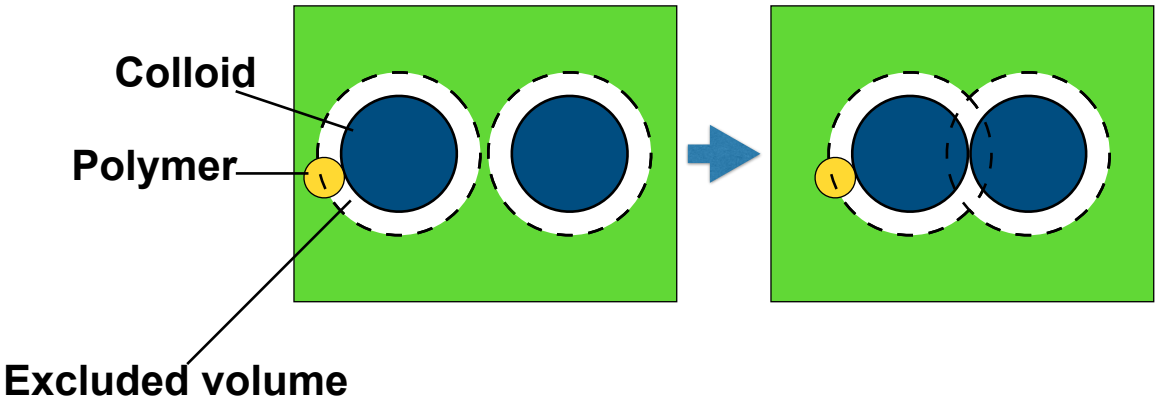

Figure 1.4: The blue disks show the colloids. The yellow disk shows the polymer. The dashed line shows the excluded volume for the center of polymer. The center of polymer can be distributed in green region. The green area is wider when the colloidal particles are in contact (right) than when they are apart (left).

1.1.4 Phase separation induced by depletion effect

The phase separation of molecules driven by the depletion effect was shown by the following research. Vrij et al. mix silica particles and polystyrene in cyclohexane solvent [10,11]. The silica particle is the colloid particle, and the polystyrene is the polymer. Experimental results show that as the concentration of polystyrene increases, phase separation occurs into two fluids with high and low concentrations of colloidal particles. The eq. (1.14) shows that as the polymer density increases, the depletion force becomes more attractive. Therefore, the phase separation is induced as the concentration of the polymer increases. They calculated the second virial coefficients using the AO theory, and explained the relationship between the phase separation and cyclohexane concentration [11].

After this research, some researchers attempt to theoretically determine the phase diagram of colloidal particles and polymers two-component systems. In 1983, Gast et

al. obtained the phase diagrams using thermodynamic perturbation theory [12]. They modeled colloidal particles as hard spheres and obtained the free energy of the hard sphere one-component system. They obtained the effective potential between colloidal particles arising from the depletion effect of polymers using the AO theory. The free energy of the hard sphere one-component system is a reference. The change in free energy from the reference is evaluated by perturbatively incorporating the above AO potential. The AO potential was obtained by substituting the experimental concentration of polymers and the experimental diameter of colloidal particle and polymer to eq. (1.13) and (1.14). The free energy of the colloidal particle effective one-component system with polymer depletion effects was obtained. The phase diagrams were obtained by constructing the common tangent on the free energy curves (FIG. 1.5 and 1.6). When the diameter of the polymer is smaller than that of the colloidal particles by 0.2 times, no first-order transition of the fluid and fluid phases is observed(FIG. 1.5). On the other hand, the transition between fluid and solid phases occurs. When the diameter of the polymer is 0.4 times larger than the diameter of the colloidal particles, fluid–fluid and fluid–solid first-order transitions occur (FIG. 1.6). In both cases, as the concentration of the polymer increases, the two-phase coexistence region expands, and the coexistence region appears at a low colloidal particle packing fraction. These results agree with the experimental results conducted by Vrij [10, 11] qualitatively.

In the early 1990s, the phase diagrams of the colloidal particle–polymer two-component systems were obtained by Lekkerker et al. [13,14] using a method different from thermodynamic perturbation theory. Their theory is called free volume theory (FVT). The reservoir of the polymer is assumed in FVT. The colloidal particle–polymer two-component system is connected to the reservoir. That is, the chemical potential of the polymer in the two-component system is constant. The free energy of this two-component system is the semigrand potential Ω. The Ω is calculated using the Legendre transformation of Helmholtz free energy, F, as follows:

$$\Omega\left(N_{\mathrm{c}}, V, T, \mu_{\mathrm{p}}\right) = F\left(N_{\mathrm{c}}, N_{\mathrm{p}}, V, T\right) - \mu_{\mathrm{p}} N_{\mathrm{p}}, \tag{1.15}$$

where N_{c} is the number of colloidal particles, N_{p} is the number of polymers, V is the volume of the two-component system, T is the temperature, μ_{p} is the chemical potential of the polymer. Using the FVT, Ω is calculated as follows:

$$\Omega\left(N_{\mathrm{c}}, V, T, \mu_{\mathrm{p}}\right) = F_0\left(N_{\mathrm{c}}, V, T\right) - p^{\mathrm{res}}\left\langle V_{\mathrm{free}}\right\rangle, \tag{1.16}$$

where F_0 is the Helmholtz free energy for a pure colloidal particle system, P^{res} is the pressure for the reservoir, and $< V_{\mathrm{free}} >_0$ is the volume where the center of the polymer can be distributed in the colloidal particle pure system. An approximation is adopted in the FVT. The approximation is that $< V_{\mathrm{free}} >$, the volume where the center of the polymer can be distributed in the two component system, is replaced by $< V_{\mathrm{free}} >_0$. $< V_{\mathrm{free}} >_0$ is obtained using scaled particle theory.

Lekkerker et al. obtained the pressure and the chemical potential of colloidal particles differentiating $\Omega(N_{\mathrm{c}}, V, T, \mu_{\mathrm{p}})$. When some phases coexist, the pressure and the chemical potentials are equal between the phases. They obtained the phase diagrams using the law. The phase diagrams obtained using the FVT are in good agreement with that obtained using the AO potential and thermodynamic perturbation theory. As the polymer packing fraction increases, the two-phase coexistence region expands, and phase separation occurs at lower colloidal particle packing fractions. This result agrees with the experiment qualitatively. When the diameter ratio of the polymer to the colloidal particle, $\sigma_{\mathrm{p}}/\sigma_{\mathrm{c}}$, is smaller than 0.32, the fluid-fluid phase separation does not occur, but the fluid-solid phase separation does. When the diameter ratio is larger than 0.32, the fluid–fluid and fluid–solid phase separation occur. It is noteworthy that at the size ratio

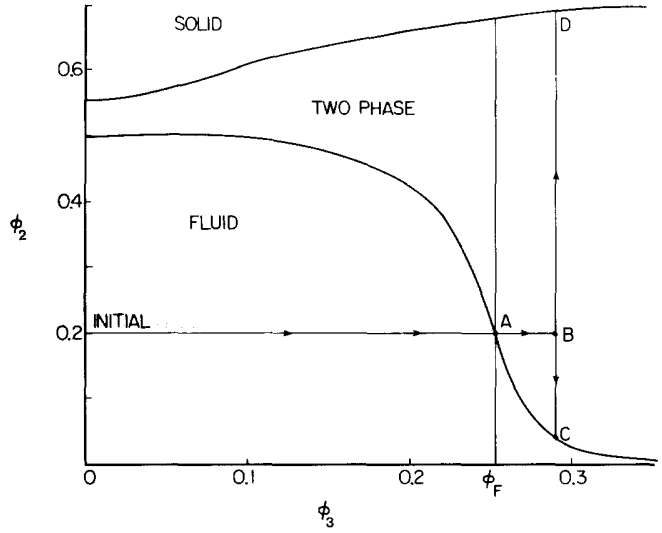

Figure 1.5: Phase diagrams calculated using the AO potential and the thermo dynamic perturbation theory. The diameter of the colloid particle is 2.5 times larger than that of the polymer. Reprinted from ref [12], Copyright (1983), with permission from Elsevier. https://doi.org/10.1016/0021-9797(83)90027-9

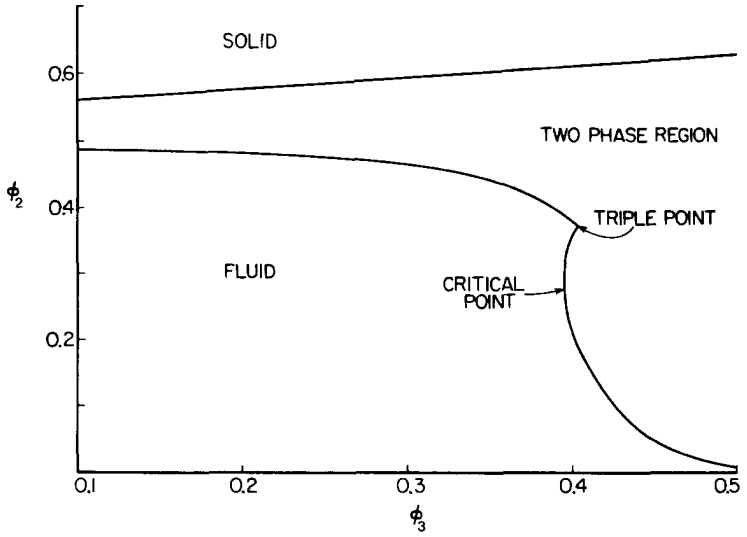

Figure 1.6: Phase diagrams calculated using the AO potential and the thermo dynamic perturbation theory. The diameter of the colloid particle is 5 times larger than that of the polymer. Reprinted from ref [12], Copyright (1983), with permission from Elsevier. https://doi.org/10.1016/0021-9797(83)90027-9

of 0.32, three phases of colloidal particles are predicted to coexist at a certain polymer packing fraction: a dilute fluid phase, a dense fluid phase, and a solid phase of colloidal particles.

The phase diagram obtained using FVT was compared with experiments [15]. The FVT indicates that fluid-fluid phase separation occurs as the value of the diameter ratio increases. To confirm this prediction experimentally, three different polymers are mixed with the colloidal particles. The diameter ratios, σ_p/σ_c, are 0.08, 0.24, and 0.57. For the diameter ratio of 0.08, the fluid–fluid phases transition is not observed. When the

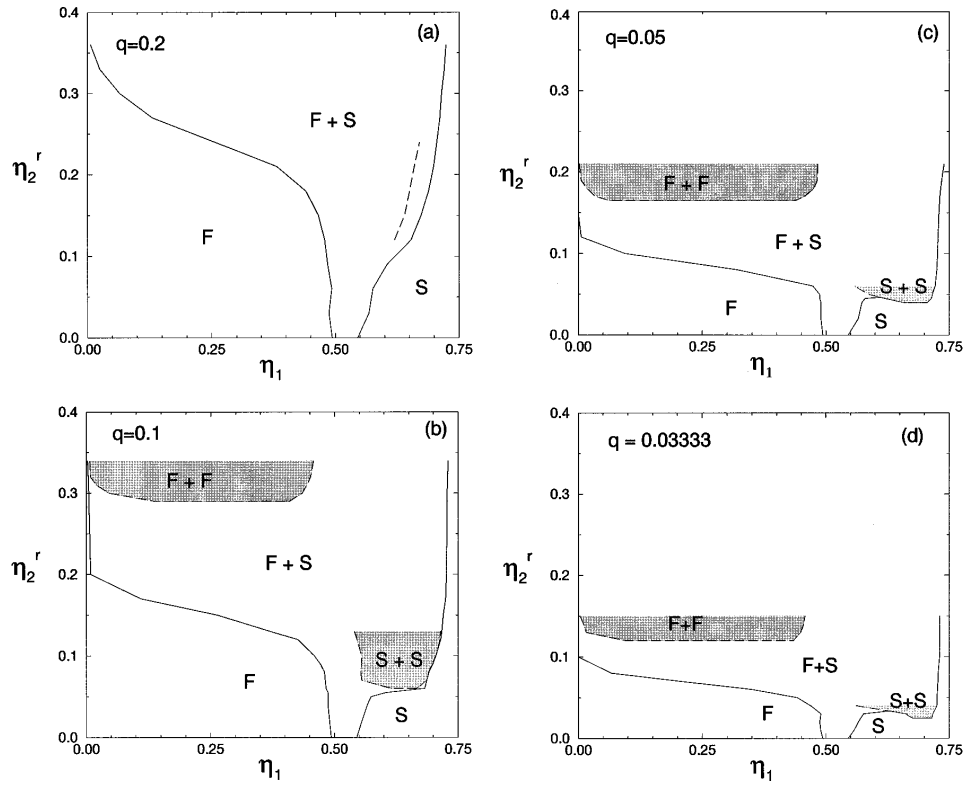

Figure 1.7: Phase diagrams obtained by simulation. The y axis is the small particle packing fraction and the x axis is the large particle packing fraction. (a) Phase diagram when the diameter ratio σ_S/σ_L is 0.2. (b) Phase diagram when the diameter ratio σ_S/σ_L is 0.1. (c) Phase diagram when the diameter ratio σ_S/σ_L is 0.05. (d) Phase diagram when the diameter ratio σ_S/σ_L is 0.03333. Reprinted figure with permission from ref. [20]. Copyright (1999) by the American Physical Society. https://doi.org/10.1103/PhysRevE.59.5744

diameter ratio is larger than 0.24, the fluid–fluid phases transition is observed. As the theory predicts, the fluid–fluid phase separation occurs when the diameter ratio increases. Therefore, FVT is valid qualitatively.

In the previous section, the statistical mechanics theories are used to predict the phase-separation behavior, but those theories contain various approximations. Therefore, researchers considered conducting a simulation that has less approximation and comparing the phase diagrams with that obtained theoretically. The phase diagrams for the two-component system of large and small hard spheres were obtained using Monte Carlo simulation [16–21] (FIG. 1.7). Comparing the phase diagrams with those obtained using the thermodynamic perturbation theory or FVT, the phase diagrams are in good agreement. Therefore, the perturbation theory and FVT are valid quantitatively.

The FVT shows that there are fewer polymers in the solid phase and in the dense fluid phase of colloidal particles. This suggests that the colloidal particles and the polymers also separate along with the phase separation of colloidal particles. That is, the separation between the colloidal particles and polymers is driven by the depletion effect. In conclusion, these series of studies showed that the separation of substances can be driven not only by energy but also by entropy.

1.2 Formation of ordering structure and liquid structure driven by repulsive interaction

1.2.1 Formation of ordering structure driven by repulsive interaction: Alder transition

The phase transition between fluid phase and ordered phase, such as solid phase, is frequently discussed focusing on the direct attractive interaction between molecules. For example, water turns into ice when the water is cooled. The reason for this is discussed as follows. The contribution of entropy to the free energy decreases as the temperature decreases. Thus, the energy becomes dominant, and drives the ordering of water molecules. In the above discussion, the isobaric condition is assumed implicitly. However, the ordering structure formation can be discussed more clearly in the isometric condition. In the isometric condition, fluid—solid phase transition can occur even when all interactions between molecules are repulsive. For example, phase transition in the binary hard sphere system is discussed. There are two species of spheres, large spheres and small spheres in the system. The spheres cannot overlap each other. The fluid—solid phase transition of large spheres occurs as the packing fraction of small spheres increases in the isobaric condition. This is because the effective attractive forces between the large spheres arise due to the depletion effect of small spheres. This was explained in the previous section. Similarly, in the hard sphere one-component system, fluid–solid phase transition occurs as the packing fraction increases. In 1962, Alder et al. showed this phase transition using computer simulation [22]. They investigated the relationship between pressure and packing fraction in a two-dimensional hard disk one-component system and confirmed that a van der Waals loop appears. Furthermore, the ordered structure of the disks was observed when the packing fraction was high. This phase transition is called the Alder transition.

The energy does not contribute to the free energy for the Alder transition because there is no direct attractive interaction. That is, the reason for the Alder transition is that the entropy for the ordered phase is higher than that for the fluid phase as the packing fraction increases. If the fluid phase remains a single phase with a high packing fraction, it seems that there are partially high and low particle packing regions. The disks hardly move in the high packing region, whereas the disks freely move in the low packing region. On the other hand, in the ordered phase, disks are evenly distributed, and the range of motion is evenly distributed. According to Boltzmann's principle, entropy is a measure of the number of microstates. It seems that the number of microstates, i.e. the arrangement of the disks, is larger when the range of motion is evenly distributed.

1.2.2 Discussion on the Alder transition based on the free volume

The Alder transition also can be discussed based on free volume. The free volume is the system volume without the excluded volume (the green region in FIG. 1.4). That is, the free volume is the volume where the center of a hard particle can be distributed. The Helmholtz free energy, F, can be calculated using the free volume. The F is

$$\frac{\beta F v_0}{V} = \int_0^{\phi} \beta\mu(\phi')d\phi', \tag{1.17}$$

where β is the inverse temperature, v_0 is volume of one particle, V is volume of the system, μ is the chemical potential, and ϕ is the packing fraction. In a three-dimensional hard sphere system, the chemical potential is calculated using the Widom insertion theorem as follows:

$$\beta\mu = \ln\Lambda^3 + \ln\frac{N}{\langle \mathrm{V}_{\mathrm{free}} \rangle}, \tag{1.18}$$

where Λ is the de Broglie wavelength, and N is the number of spheres. Substituting the eq. (1.18) to eq. (1.17), the Helmholtz free energy in the three-dimensional hard sphere is as follows:

$$\frac{\beta F v_0}{V} = \phi \ln \frac{\Lambda^3}{v_0} + \phi \ln \phi - \phi - \int_0^{\phi} \ln \frac{\langle V_{\text{free}} \rangle}{V} d\phi. \tag{1.19}$$

Comparing the free energies in the fluid and solid phases at the same packing fraction, the reason for the Alder transition is predicted as follows. The free energy in the solid phase should be higher than that in the fluid phase when the packing fraction is low. On the other hand, the free energy in the solid phase should be lower than that in the fluid phase when the packing fraction is high. Eq. (1.19) shows that the free energy decreases as the free volume decreases. Therefore, this reversal occurs because the free volume fraction, $< V_{\text{free}} > /V$, in the solid phase is smaller than that in the fluid phase at the high packing fraction.

To confirm the large–small relation change of the free volume fraction between the fluid and solid phase, the free volume fraction is calculated by scaled particle theory (SPT) [23, 24] as follows:

$$\frac{\langle V_{\text{free}} \rangle}{V} = (1-\phi) \exp \left[\frac{-6\phi}{1-\phi} - \frac{9\phi^2}{2(1-\phi)^2} - \beta p v_0 \right], \tag{1.20}$$

where p is the pressure. The pressure for the fluid phase is calculated by SPT [23, 24] as follows:

$$\beta p_{\text{flu}} v_0 = \frac{\phi + \phi^2 + \phi^3}{(1-\phi)^3}. \tag{1.21}$$

The pressure for the solid phase is calculated by cell theory [24, 25] as follows:

$$\beta p_{\text{sol}} v_0 = \frac{3\phi}{1 - \frac{\phi}{\phi_{\text{cp}}}}, \tag{1.22}$$

where ϕ_{cp} is the close packing (≈ 0.74). The free volume fraction for the fluid and solid phases are shown in FIG. 1.8. FIG. 1.8(a) shows that the free volume fraction in the fluid phase is larger than that in the solid phase in the low packing fraction, whereas the free volume in the fluid phase is smaller when the packing fraction is higher than about 0.4. These results agree with the prediction using eq. (1.19). However, the FIG. 1.8(b) shows that the free volume in the fluid is larger again when the packing fraction is larger than about 0.7. The solid must not melt as the packing fraction increases in the real system. Therefore, the SPT seems to give an incorrect free volume fraction in the fluid phase at the high packing fraction. At the close packing, the pressure must be infinity, and the free volume must be 0. Actually, in the solid phase, the eqs. (1.20) and (1.22) show that the pressure is infinity, and the free volume is 0 at the close packing. However, in the fluid phase, the pressure calculated by SPT has a finite value, and the free volume calculated by SPT is not 0 at the close packing. Therefore, the SPT is not valid for $\phi \approx 0.74$. The validity is also uncertain for $0.49 < \phi < 0.54$ where the Alder transition occurs. To examine the validity, fluid–solid phase coexistence region is obtained by calculating the Helmholtz free energies for the fluid and solid phases, F_{flu} and F_{sol}, as follows:

$$\frac{\beta F_{\text{flu}} v_0}{V} = \phi \ln \left[\frac{\Lambda^3}{v_0} \right] + \phi \ln \left[\frac{\phi}{1-\phi} \right] - \frac{5}{2}\phi + \frac{3}{2} \frac{\phi}{(1-\phi)^2} \tag{1.23}$$

$$\frac{\beta F_{\text{flu}} v_0}{V} = \phi \ln \left[\frac{\Lambda^3}{v_0} \right] + \phi \ln \phi + (1-\phi) \ln (1-\phi) - \frac{3}{2}\phi + \frac{9}{2(1-\phi)} + 3 \ln [1-\phi]$$
$$- 3\phi_{\text{cp}} (\phi_{\text{cp}} \ln [\phi_{\text{cp}} - \phi] + \phi) - \frac{9}{2} + 3\phi_{\text{cp}}^2 \ln \phi_{\text{cp}} \tag{1.24}$$

I calculated $\ln\left[\Lambda^3/v_0 = 0\right]$ because this term does not affect the phase diagram. The Helmholtz free energies are shown in FIG. 1.9 (a). The phase coexistence region is obtained by common tangent construction (FIG. 1.9 (b)). The coexistence region is $0.475 < \phi < 0.495$. The reported coexistence region obtained using simulation is $0.494 < \phi < 0.545$ [26]. The calculated result is in good agreement with that obtained using simulation. Thus, the SPT is valid for the calculation of the Alder transition. Therefore, the Alder transition occurs because the free volume fraction in the solid phase is larger than that in the fluid phase when ϕ is larger than about 0.4.

When the molecules are crowded, the space where a new molecule can be inserted is small. That is, the free volume fraction is small. On the other hand, when the molecules are almost empty, the free volume fraction is large. Thus, the free volume fraction corresponds to the crowding of the molecules. Therefore, the Alder transition shows that the crowding of molecules can be the critical factor for the fluid—ordered phase transition.

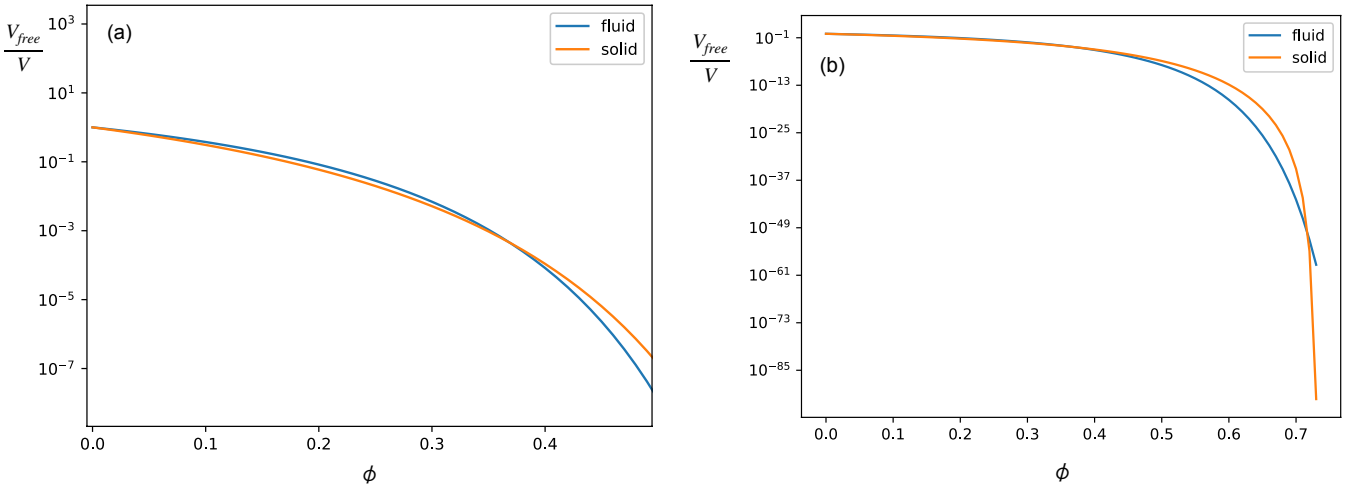

Figure 1.8: The y axis shows the free volume fraction. The x axis shows the packing fraction. (a) The free volume fraction is shown for $\phi < 0.5$. (b) The free volume fraction is shown for $\phi < \phi_{cp}$.

1.2.3 Formation of liquid structure driven by repulsive interaction: van der Waals picture

The crowding is also critical for the formation of liquid structure. In this section, the isotropic particles one component system is assumed. Here, the liquid structure means the average number of particles surrounding one particle. The radial distribution function is useful to express the liquid structure. The radial distribution function, $g(r)$, is defined as follows:

$$g(r) \equiv \frac{\rho^{(2)}(r)}{\rho^2}, \tag{1.25}$$

where $\rho^{(2)}(r)$ is the probability that a particle is at a position r away from any particle. ρ is the total number density of the system. I will explain the meaning of $g(r)$. The eq. (1.25) can be transformed to as follows:

$$\rho g(r) = \frac{\rho^{(2)}(r)}{\rho}, \tag{1.26}$$

where the ρ can be interpreted as the probability that a particle is at the origin of a coordinate. The right side of the eq. (1.26) can be interpreted as a conditional probability.

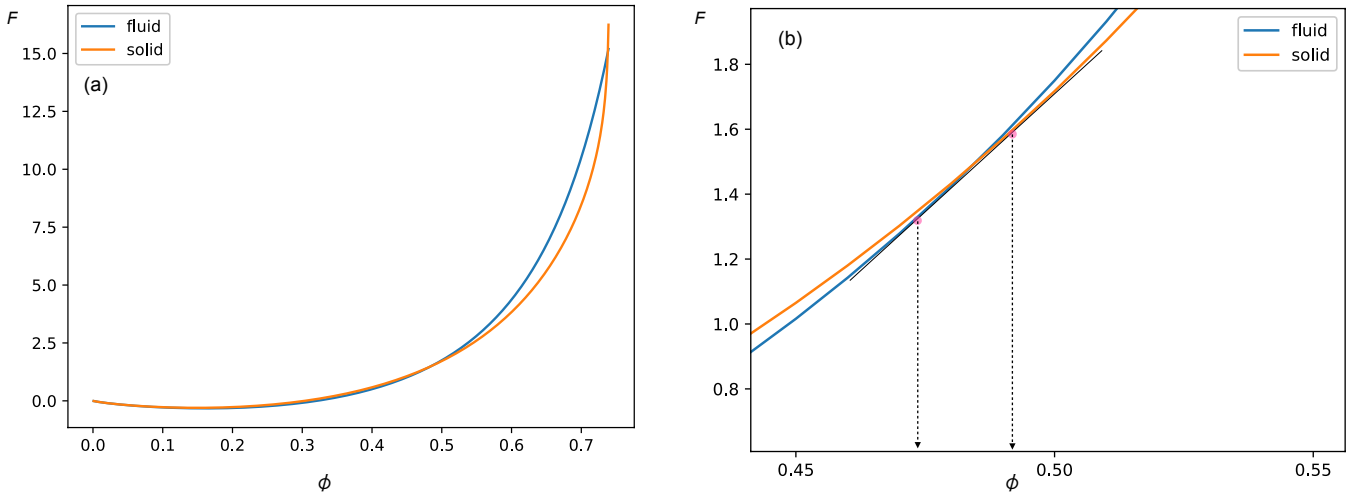

Figure 1.9: (a) The Helmholtz free energy fir the fluid phase (blue curve) and the solid phase (orange curve). (b) The common tangent on the free energy curves. The dotted arrows show the coexistence region.

That is, the right side of the eq. (1.26) shows the probability that when any particle is at the origin, another particle is at a position r away from the origin. In other words, the eq. (1.26) shows the number density of particles at a position r away from the origin when a particle is at the origin. This expresses the liquid structure. Therefore, the radial distribution function is useful to express the liquid structure.

The condensed system under isochoric condition is discussed. A picture of the condensed system was proposed. The picture asserts that the repulsive interaction between molecules is dominant for liquid structure formation. This picture is a part of the “ van der Waals picture ”. I explain how this picture was shown. Chandler et al. divided the Lennard-Jones potential into a repulsive and an attractive terms. They showed that just the repulsive term reproduced the radial distribution function of Lennard-Jones fluid [27–29]. Therefore, the repulsive interaction is dominant for the liquid structure formation. The details are as follows. The Lennard-Jones potential, $\omega(r)$, is

$$\omega(r) = 4\varepsilon\left[\left(\frac{r}{\sigma}\right)^{12} - \left(\frac{r}{\sigma}\right)^{6}\right], \tag{1.27}$$

where r is the distance between centers of Lennard-Jones particles, ε and σ is fitting parameters. This potential is shown in the left side of FIG. 1.10. The potential has a minimum at the distance, $r_0 = 2^{\frac{1}{6}}\sigma$. The attractive force works between the particles at the $r > r_0$. On the other hand, the strong repulsive force works between the particles at the $r < r_0$. Chandler et al. divided the Lennard-Jones potential into a repulsive and an attractive terms. The repulsive term, $u_0(r)$, is as follows:

$$u_0(r) = \omega(r) + \varepsilon \qquad r < r_0, \tag{1.28}$$

$$u_0(r) = 0 \qquad r \leq r_0. \tag{1.29}$$

The attractive term, $u(r)$, is as follows:

$$u(r) = \omega(r) - u_0(r). \tag{1.30}$$

The $u_0(r)$ and $u(r)$ are shown in the right side of FIG. 1.10.

The radial distribution function shows the structure of the liquid. Chandler et. al. calculated the radial distribution function, $g_0(r)$, for the repulsive term of Lennard-Jones

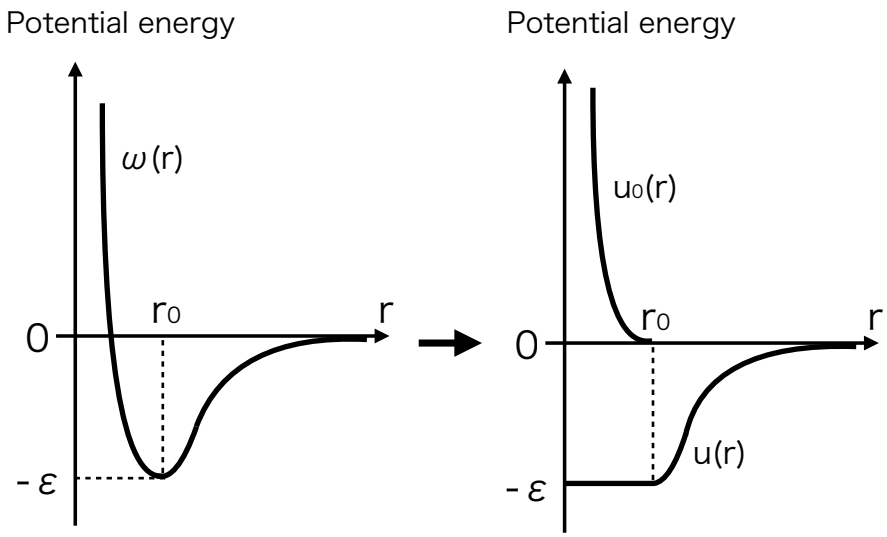

Figure 1.10: The left side shows the Lennard-Jones potential. The right side shows the repulsive term, $u_0(r)$, and the attractive term, $u(r)$, of Lennard-Jones potential.

potential, $u_0(r)$. They compared $g_0(r)$ with that for the Lennard-Jones potential, $g(r)$ [27]. $g_0(r)$ agree with $g(r)$, although $u_0(r)$ does not contain the attractive term. Thus, the repulsive interaction seems to be dominant for the liquid structure. In addition, $g_0(r)$ is also in good agreement with the radial distribution function for the hard spheres, $g_d(r)$ [27]. Thus, the softness of the Lennard-Jones potential seems to have less influence on the liquid structure.

The van der Waals picture can be interpreted as that the particles form the structure colliding with each other in the liquid. That is, the crowding is critical for the structure of the liquid. However, the reference [27] pointed out that when electronic interactions are strong or hydrogen bonds are formed, the attractive part is critical, and the van der Waals picture is not correct. The crystallization of bacteriorhodopsins (bRs) in a bio membrane is discussed in this thesis. The transmembrane domain of bR is composed of hydrophobic amino acid, and most of the bR is composed of transmembrane domain. Therefore, the interactions between the transmembrane domains seem to be dominant for the crystallization. It has not been reported that the ion bond or the hydrogen bond is formed between the transmembrane domains. In addition, the biomembrane is a condensed system of lipid molecules. The number density of lipid molecules is 2.5×10^6 μm^{-2} in a single layer of a cell membrane [30]. When the diameter of the lipid molecule is modeled as 0.5 nm, the packing fraction of the lipid molecules is 0.5, which is a very crowded system of lipid molecules. Therefore, I consider that the van der Waals picture is valid for the discussion of bR crystallization, and the repulsive force is dominant for the crystallization.

1.3 Phase transition in two-dimensional hard disk system

In this section, phase transition in a two-dimensional hard disk system is explained. The Bacteriorhodopsin (bR) has an almost cylindrical shape, and the top and bottom of the bR are exposed to water. On the other hand, the side of bR consists of hydrophobic amino acids, and the side is covered by lipid molecules. Thus, the vertical motion of the bR to the membrane seems to be energetically unfavorable as it exposes the hydrophobic region of the bR to the water. Therefore, the motions of bRs seem to be limited to the lateral direction. That is, the system of transmembrane proteins in a membrane can be regarded as a condensed system in which the degrees of freedom are generally limited to the two-dimensions. For this reason, I modeled the crystallization of the bRs as a phase transition of hard disks in the 2D system. However, phase transition in the 2D systems differs from that in the 3D system in some respects. Therefore, it is questionable to discuss the 2D phase transition with the same way as the 3D phase transition. For example, I explain the phase transition for hard spheres and hard disks one component system, which is regarded as a reference system for a binary system. In the 3D system, the fluid—solid first order phase transition occurs [31, 32]. On the other hand, in the 2D system, there is an additional phase, namely the hexatic phase, between the fluid and solid phases [33–35]. That is, the fluid–hexatic first phase transition occurs instead of the fluid–soild phase transition. When the first order transition of the fluid—solid phases is assumed in the 2D system, the validity for the theoretical results is uncertain. Therefore, it is questionable to construct theories for the 2D phase transition with the same way as the theories for the 3D phase transition. However, according to a reference [36], the hexatic phase disappears, and the fluid—solid first order transition also occurs in the 2D binary hard disk system. Therefore, I considered that the 2D theories of the depletion effect can be constructed with the same way as that for the 3D theories.

1.3.1 Characteristics of the fluid, hexatic, solid phases

I will explain the hexatic phase. The hexatic phase has characteristics intermediate between the fluid phase and the solid phase. Here, it is hard to distinguish the hexatic phase and solid phase by their appearance. Thus, it is useful to distinguish each phase by bond orientational correlation and positional correlation. The characteristics of the fluid phase, the hexatic phase, and the solid phase will be shown, respectively.

The bond orientational order, ψ_6, is defined as follows:

$$\psi_6 \equiv \frac{1}{N}\Sigma_k \exp\left[6\mathrm{i}\theta_{\mathrm{jk}}\right], \tag{1.31}$$

where N is the number of disks that surround a disk "j", "k" is a disk surrounding the "j", and θ_{jk} is the angle formed by a reference axis and a line connecting the centers of the disks "j" and "k". When the disks form a perfect hexagonal lattice, $|\psi_6|$ is 1. As the hexagonal lattice collapses, $|\psi_6|$ decreases. Each phase is characterized by the length of bond orientational correlation. The bond orientational correlation function, $C_6(r)$, is defined using ψ_6 as follows:

$$C_6(r) = \left\langle \psi_{6i}\psi_{6j}^* \right\rangle, \tag{1.32}$$

$$r = |\boldsymbol{r}_j - \boldsymbol{r}_i|, \tag{1.33}$$

where ψ_{6i} and ψ_{6j} are the bond orientational order for disks "i" and "j", respectively, and $\boldsymbol{r}_i$ and $\boldsymbol{r}_j$ are the position vector for "i" and "j". In the fluid phase, the bond orientational correlation function decreases exponentially to 0. In the hexatic phase, that function decreases algebraically to 0. In the solid phase, that function decreases algebraically

approaching contact value. In other words, the bond orientational correlations for the fluid, hexatic, and solid phases are short ranged, quasi-long ranged, and long ranged, respectively.

I will explain the positional correlation function. The positional correlation function is obtained from the spatial correlation function, $g(\Delta x, \Delta y)$. This function is like the radial distribution function explained in section 1.2.3. However, the variable is not the distance, r, but the coordinates, Δx and Δy. The spatial correlation function, $g(\Delta x, \Delta y)$, is as follows:

$$g(\Delta x, \Delta y) = \frac{\rho^{(2)}(\Delta x, \Delta y)}{\rho^2}, \tag{1.34}$$

where $\rho^{(2)}(\Delta x, \Delta y)$ is the probability that a particle is at a position Δx and Δy away from any other particle. ρ is the total number density for the system. In the hexatic and solid phases, the maxima of the correlation function line up in a lattice-like pattern (see FIG. 1.12 (a)). The positional correlation function is the spatial correlation function in the direction where the distance between the maxima is approximately the particle diameter (see the white line in FIG. 1.12 (a)). In the fluid and hexatic phases, the positional correlation function decreases faster than $r^{\frac{-1}{3}}$, i.e. the positional correlation is short ranged. On the other hand, in the solid phase, that function decreases algebraically to 0 slower than $r^{\frac{-1}{3}}$, i.e. the positional correlation is quasi-long ranged.

1.3.2 Fluid—hexatic first order phase transition and hexatic—solid continuous phase transition

It is now considered that the phase transition from the fluid phase to the solid phase occurs via the hexatic phase. However, there had long been controversy over whether these phase transitions are continuous or discontinuous. In 2011, the phase transition for the hard disks in the 2D one component system was examined. Krauth et. al. conducted event chain Montecarlo simulation (ECMC) on the 2D hard disk system [37]. The ECMC is rejection free algorithm, i.e. the displacement of a disk always occurs without rejection. Therefore, the time for equilibration is shorter than the metropolis method. In addition, the pressure is easily calculated by the ECMC. When the phase transition is calculated by simulation, the system size is much smaller than experiments, and the boundaries between the two phases affect the phase transition, unlike the experiment. That boundary effect become smaller as the system size is larger. That is, the system size affects the phase transition in the simulation. Krauth et. al. simulated the very large system where the number of disks was 1024^2 to reduce the system size effect. The pressures were examined at various packing fractions. The result shows the van der Waals loop and it indicates that the first order phase transition occurs (FIG. 1.11). The pressure is constant during the first order phase transition in the isometric process. On the other hand, the van der Waals loop appears due to the system size effect in a simulation. Actually, the loop approaches the horizontal line to the x axis as the system size increases to 256^2, 512^2, and 1024^2. The two phases coexistence region was obtained by adopting Maxwell equal area rule on the loop. The packing fraction of the phase coexistence region is from 0.700 to 0.716. The coexistence region is the fluid—hexatic phase coexsistence region. In addition, they examined the positional correlation function (FIG. 1.12 (b)). When the packing fraction is 0.718, the positional correlation function decreases exponentially. It indicates the hexatic phase. On the other hand, when the packing fraction is 0.720, the positional correlation decreases algebraically. It indicates the solid phase. In this phase transition, the van der Waals loop was not observed. It indicates that the hexatic—solid phase transition is continuous. In conclusion, the phase diagram for the 2D hard disk one component system is FIG. 1.13. The correctness for this phase diagram was confirmed by other simulation methods [38].

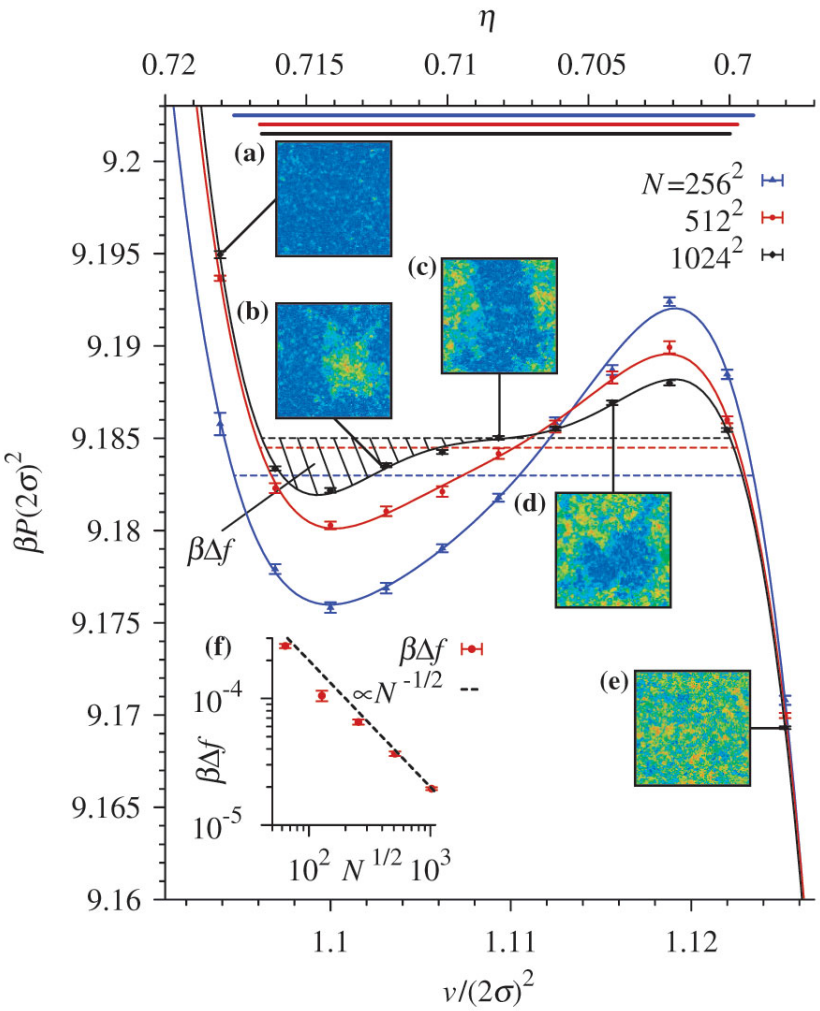

Figure 1.11: The van der Waals loop calculated by ECMC. The y axis is the pressure scaled by temperature and diameter of disk. The x axis is volume per particle scaled by diameter of disk. The blue, red, and black curves show the pressure when the system size is $N = 256^2$, $N = 512^2$, and $N = 1024^2$, respectively. Reprinted figure with permission from ref. [37]. Copyright (2011) by the American Physical Society. https://doi.org/10.1103/PhysRevLett.107.155704

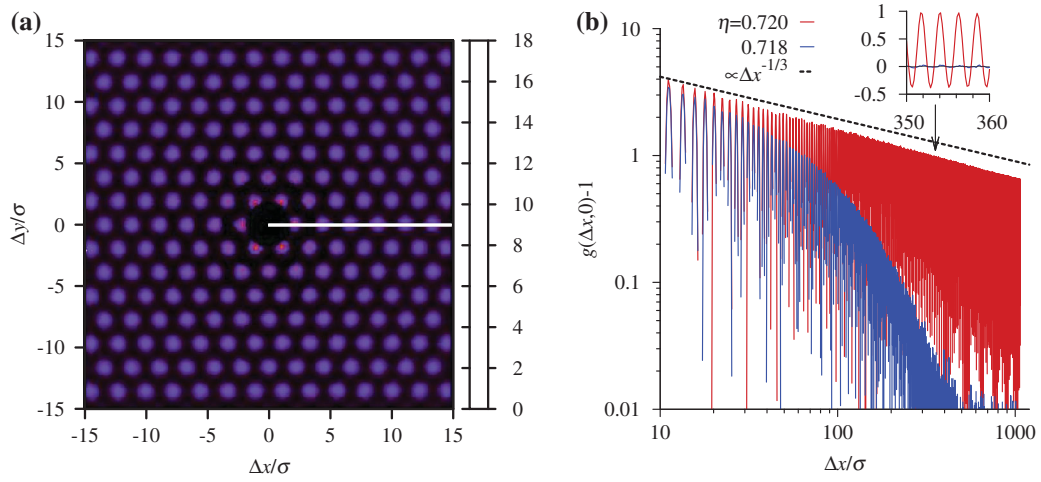

Figure 1.12: (a) A spatial correlation function when the packing fraction is 0.718. (b) The positional correlation function when the packing fraction is 0.718 (blue line) and 0.720 (red line). Reprinted figure with permission from ref. [37]. Copyright (2011) by the American Physical Society. https://doi.org/10.1103/PhysRevLett.107.155704

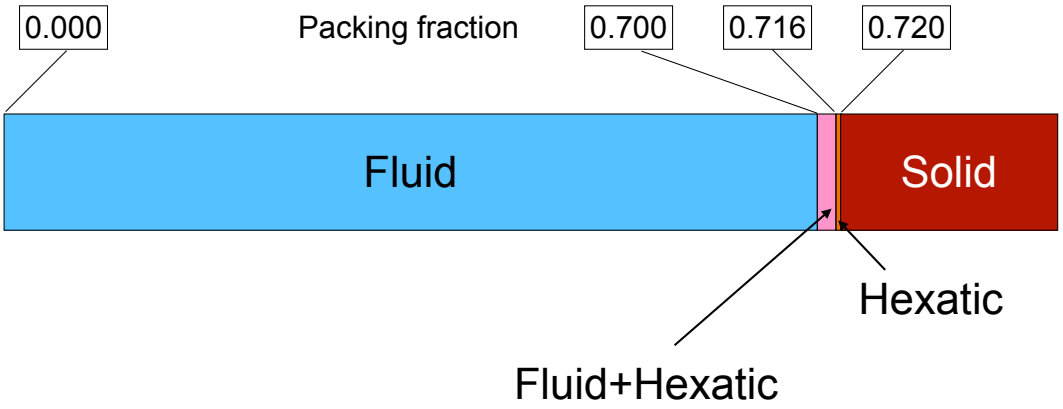

Figure 1.13: The phase diagram for the 2D hard disk one component system. The phase diagram shows single fluid phase, fluid—hexatic coexistence phase, hexatic single phase, and single solid phase from left to right.

1.3.3 Disappearance of the hexatic phase

In addition, the phase diagram for a 2D binary hard disk system was examined by using simulation. In 2017, Wilding et. al. reported that the hexatic phase disappeared in the binary hard disk system [36]. In the system, the diameter ratio between the small disk and the large disk is 1: 1.4. The total number of particles is 256^2 or 512^2. The large particle and small disk change each other according to activity. When the activity is high, the large disk easily changes to the small disk. In other words, the small disks increase as the activity increases. Wilding et. al. examined the pressures at various number densities and activities, and they obtained the van der Waals loop. They calculated the number densities for the phase coexistence region at a fixed activity from the loop. The positional correlation function was examined to distinguish the hexatic phase or the solid phase around the boundary between coexistence region and the hexatic or solid phases (FIG. 1.14(c)), and they obtained the phase diagram (FIG. 1.14(a)). The phase diagram shows that when the small disk number is larger than 1% of the total disk number, the hexatic phase disappears, and the fluid—solid first order phase transition occurs like a 3D system. I consider the reason for the disappearance of the hexatic phase as follows. In the binary hard disk system, the ordered phase of the higher large disk packing fraction appears due to the depletion force than that in the one component system. At the higher packing fraction, the solid phase seems to be more stable than the hexatic phase as is shown in FIG. 1.13.

In conclusion, there is the hexatic phase between the fluid and solid phases. The hexatic phase has intermediate characteristics between the fluid and solid phases. In the 2D hard disk one component system, the fluid—hexatic first order phase transition occurs and the hexatic—solid continuous phase transition occurs as the packing fraction increases. However, in the binary hard disk system, the hexatic phase disappears, and fluid—solid first order phase transition occurs. The reason for the disappearance seems to be the depletion effect. Therefore, I consider that in the bR-lipid two component system, the bR fluid—solid first order phase transition occurs due to the depletion effect of lipid molecules. Thus, I consider that the crystallization for the bRs can be discussed as with the 3D system. However, the simulation research which showed the disappearance of the hexatic phase was conducted with the disk diameter ratio 1 : 1.4, which was far from the diameter ratio between lipid molecule and bR, 1 : 12.4. The first order phase transition between the bR fluid—solid phase should be confirmed by the simulation.

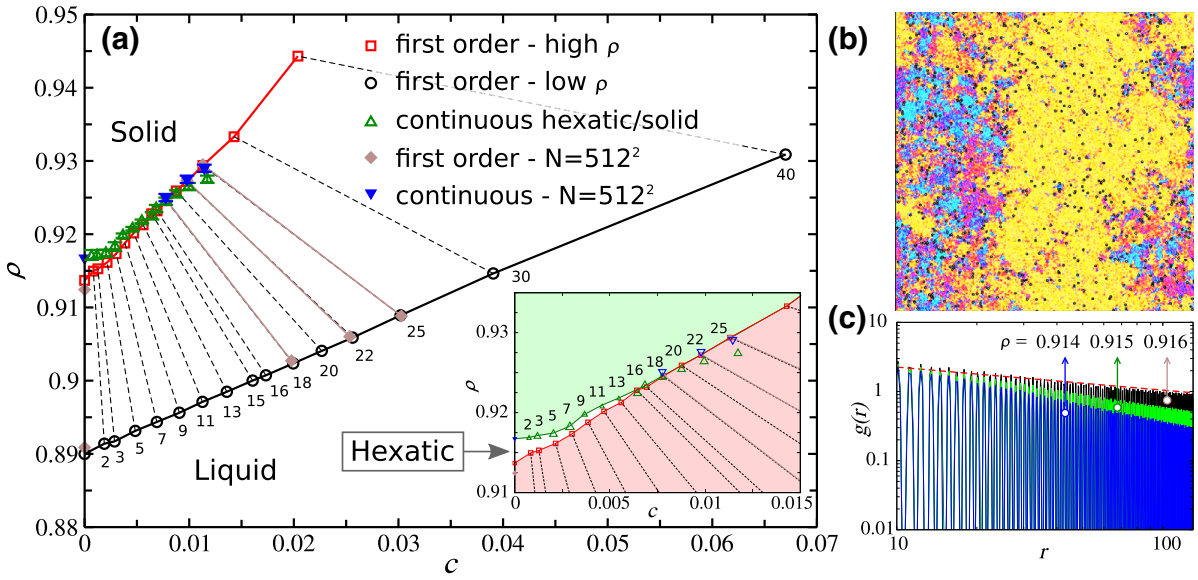

Figure 1.14: (a) Phase diagram for a binary hard disk system. The y axis is number density for all disks, ρ. The x axis is the number fraction for small disks to all disks. The value in the phase diagram shows the activity ($\times 10^{-5}$). The dotted line shows the corresponding phase transition. The red squares and black circles show the first order phase transition in the system of 256^2 particles. The green triangles show hexatic—solid continuous phase transition. The purple diamonds and blue inverted triangles show the first order and continuous phase transition, respectively in the system of 512^2 particles. (b) Snapshot when the activity is 15×10^{-5} at $\rho = 0.91$. The color is assigned by the ψ_6. (c) Positional correlation function at the $\rho = 0.914$ (blue), $\rho = 0.915$ (green), and $\rho = 0.916$ (black) when the activity is 2×10^{-5}. Reprinted figure with permission from ref. [36]. Copyright (2017) by the American Physical Society. https://doi.org/10.1103/PhysRevLett.119.115702

1.4 Crystallization of bacteriorhodopsin

In this section, previous experimental research on crystallization of bacteriorhodopsin (bR) is summarized. The bR is a transmembrane protein of *Halobacterium salinarum*. The bR functions as a light-driven proton pump. The bRs construct a two-dimensional crystal in the biomembrane. The bR crystal is called purple membrane after its color. The structure of the crystal is a hexagonal lattice. According to Mermin and Wagner, there is no perfect crystal of infinite size in the 2D system [39, 40]. As is explained in the section 3.1, the positional correlation function decreases algebraically to 0 at the infinite distance. However, the size of the biomembrane is finite, and the purple membrane consists of the limited number of the bRs. The number of bR trimers is just 6000 in one purple membrane [41]. The decrease of the positional correlation function is very small in that small solid. Therefore, I consider that the purple membrane can be regarded as the crystal. Generally, it is considered that the bR monomers first form trimers, and the trimers aggregate to construct a crystal [41]. Actually, the bR trimer apart from the crystal was observed by using high-speed atomic force microscopy [42]. This result indicates that the bR trimer can exist out of the crystal, and the result supports the hypothesis that the trimers construct the crystal.

Here, I assume the fluid—solid first order phase transition for the bR. Since the biomembrame is modeled as a two-dimensional system, there is the possibility for the fluid—hexatic phase transition. However, there are many lipid molecules in the membrane. As is explained in section 1.2.3, the number density for the lipid molecules is $2.5 \times 10^6/1\mu m^2$ in the plasma membrane of an animal cell, and the packing fraction of lipid molecules is about 0.5 when the lipid diameter is modeled as 0.5 nm. The similar lipid packing fraction is expected in the bacterial membrane. I consider that in such a condensed system with lipid molecules, the depletion effect works between the bRs. Therefore, the hexatic phase seems to disappear as described in the section 1.3.3, and the fluid–solid first order phase transition seems to occur.

1.4.1 Critical concentration ratio between bR monomer and bR trimer

In this section, I will explain the difference of crystallization between bR monomer and trimer. The bR has seven alfa helixes (FIG. 1.15(A)). Each helix is named with an alphabet. Two bR monomers contact each other at helices B and D to form a trimer (FIG. 1.15(b)). In 1997, Krebs et al. prepared mutant bRs that failed to form a trimer [43]. An amino acid present in the helix D of the mutant bR was replaced by another amino acid. There were four mutants: a mutant in which the glycine at position 113 was replaced with leucine (G113L), a mutant in which the glycine at position 116 was replaced with leucine (G116L), a mutant in which the isoleucine at position 117 was replaced with alanine (I117A), and a mutant in which the isoleucine at position 117 was replaced with phenylalanine (I117F). Each mutant bRs were expressed in *Halobacterium salinarum.* The cells were disrupted, and equilibrium gradient centrifugation was performed. The bR crystal has high density and can be separated from the cell membrane by the centrifugation. bR crystals were obtained for all mutants. CD spectra of each mutant bR crystal and wild type bR crystal were measured. The results showed no significant changes between the wild type and each mutant bRs. Low-angle X-ray diffraction revealed no significant differences between the mutant and wild-type bR crystals. For these observations, it is presumed that the mutant bR crystals have the same structure as the wild-type bR crystal and the 3D structure of the bR mutant is not significantly different from that of the wild-type bR. In addition, the CD spectra were also examined for mutant bRs that did not construct crystals (FIG. 1.16). The CD spectrum for the wild type bR trimer has maxima at about 500 nm and minimum at about 600 nm. However, the bR mutants,

G113L and I117A, do not show that spectra pattern. Their CD spectra have maxima at about 600 nm. These results indicate that G113L and I117A do not form the trimer out of the crystal. The CD spectra agree with that for bR monomer [44]. Therefore, these results indicate that G113L and I117A are in monomer form out of the crystal. On the other hand, the CD spectra for G116L and I117F have maxima at about 500 nm and minimum at about 600 nm. However, the absolute values for the maxima and minimum are smaller than those of the mutants in the crystal. These results indicate that G116L and I117F form not only the trimers but also monomers or another multimer out of the crystal.

In 1999, Krebs et. al. examined the critical concentration (CC) for mutant bRs. At the CC, the bRs start to crystallize. They compared the CC with that for wild type [45]. The experimental method is as follows. They induced the expression of the mutant or wild type bRs in the bacteria. They obtained the bacteria with different times of growth after the induction. Thus, the samples of bR crystals at different growth stages were obtained. They plotted the relationship between the weight of total bR in the bacteria (%bRt) and the weight of the bR in the crystals (%bRl) (FIG 1.17). Each value was scaled by the total protein in the bacteria. The experimental data over 0 were fitted by a linear function. When the %bRl value of the linear function is 0, the value of %bRt is the CC. I focus on the bR mutants, G113L and I117A, which are indicated not to form a trimer out of the crystal. The CC for the wild type bR is 0.24, whereas the CC for the G113L is 2.45 and the CC for the I117A is 1.65. On the other hand, the CC for the I117F, which is indicated partially form the trimer is 0.83. The CC for the I117F is higher than that for the wild type but lower than that for the G113L and I117A which do not form trimer. The CC for the G116L was not examined. For these results, the formation of the trimers seems to decrease the CC. I consider that the CC difference between the monomer, namely G113L and I117A, and trimer, namely wild type, can be explained by the depletion effect. When the bR monomers form the trimer, the diameter becomes larger than that of the monomer. Therefore, the diameter ratio between lipid and bR trimer becomes larger, and the depletion effect on the bR trimer become larger. To confirm this hypothesis, I obtained phase diagrams by using theories containing depletion effect and compared the CC between the monomer and trimer. I focused on the critical concentration ratio between monomer and trimer (CC monomer/ CC trimer) to compare the experimental results and theoretically calculated results. I adopt the CC for the monomer as 2.45, which is the CC for G113L, and the CC for the trimer as 0.24, which is the CC for wild type. Thus, the CCR is 10.2. Here, the CCR is the weight ratio of bR monomer and trimer in the same system size. The bR weight and the area which bR occupy is proportional. Therefore, the weight ratio has the same value of the area ratio between bR monomers and trimers. I calculated packing fractions of bR monomer and trimer at the beginning of crystallization and obtained CCR. The results are shown in chapter 2 and 3 in this thesis.

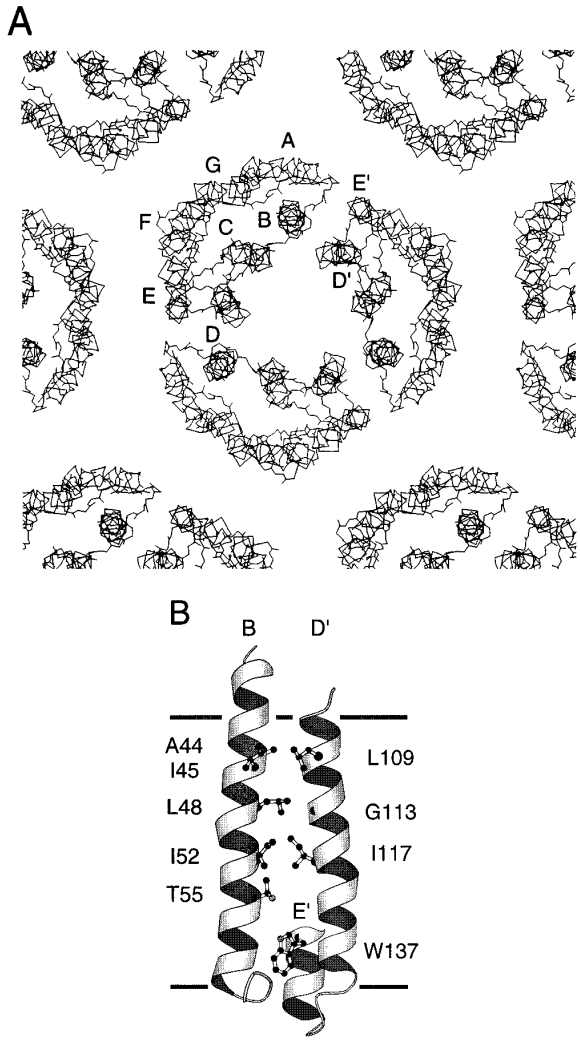

Figure 1.15: (A) bR crystal on the membrane. Seven alfa helixes are named A, B, C, D, E, F, and G. (B) Two bRs contact at helix B and D. Alphabets show the amino acid. Numbers show the order of amino acids within the protein. Reprinted with permission from [45]. Copyright 1999 American Chemical Society. https://doi.org/10.1021/bi9905563

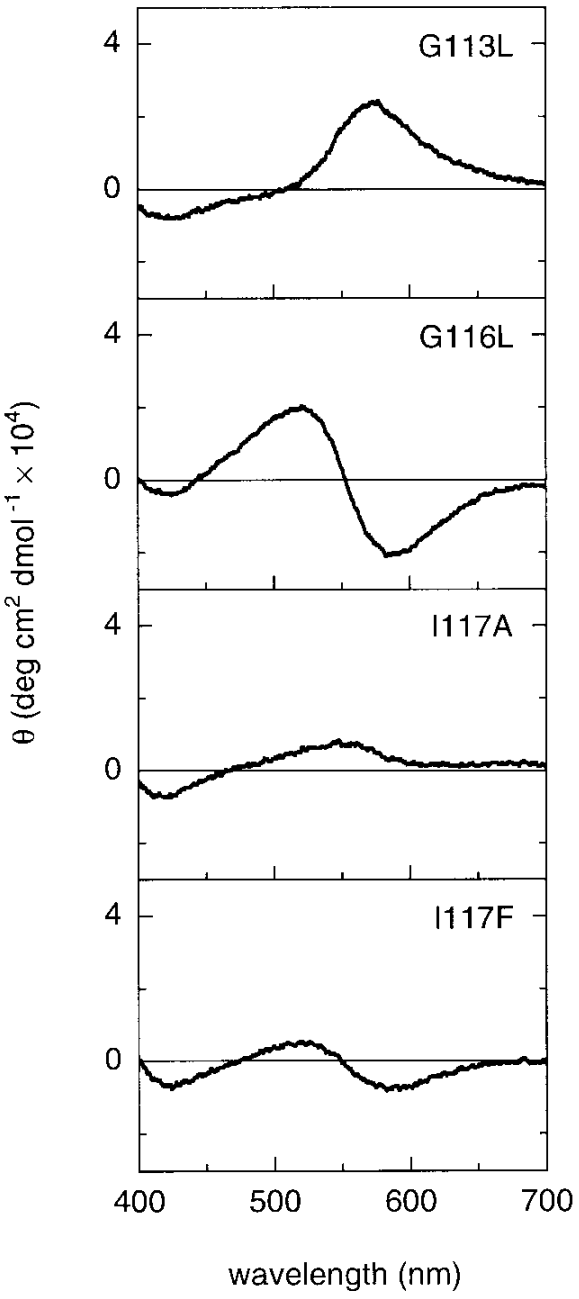

Figure 1.16: CD spectra for bR mutants. The CD spectra for G113L, G116L, I117A, and I117F are shown from top to bottom. Reprinted from ref. [43]. Copyright (1997), with permission from Elsevier. https://doi.org/10.1006/jmbi.1996.0848

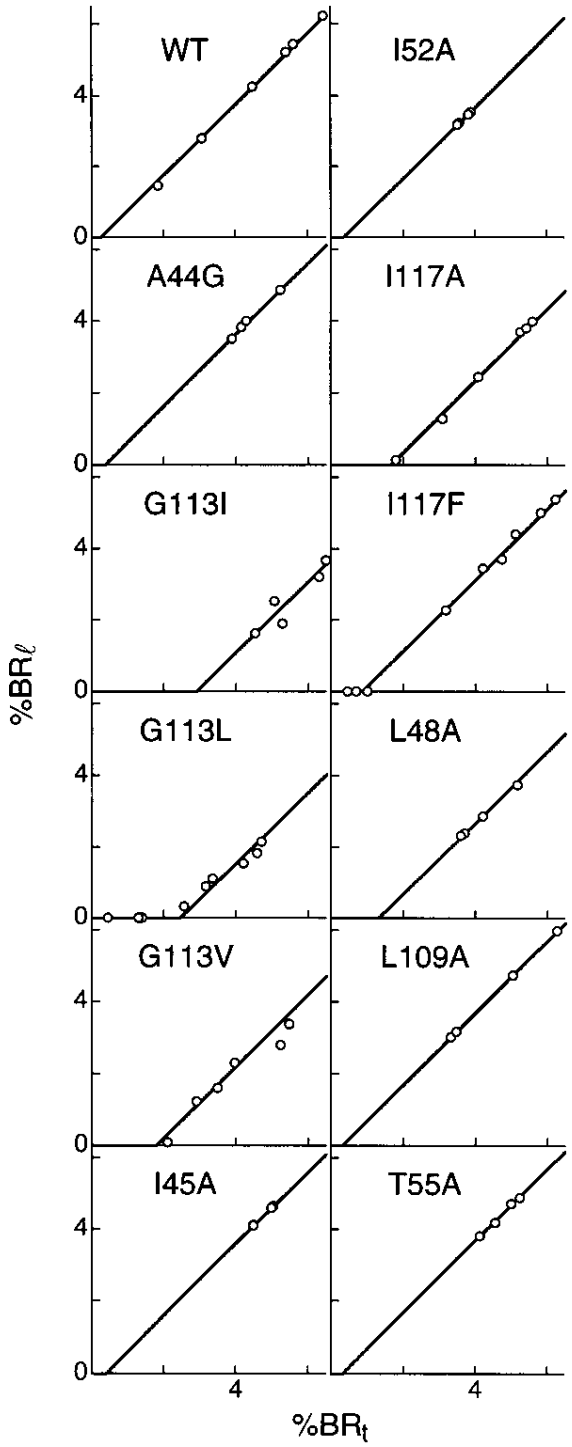

Figure 1.17: The y axis shows the bR weight in crystal. The x axis shows the total bR weight in the cell. Each value are scaled by total protein weight. Symbols show the experimental value. The experimental data are fitted by linear function. The combination of alphabet and number shows the mutant type. WT shows the wild type bR. Reprinted with permission from [45]. Copyright 1999 American Chemical Society. https://doi.org/10.1021/bi9905563

Chapter 2

Examination of two-dimensional bR crystallization driven by lateral depletion effect using two-dimensional free volume theory

The 2D ordering of bacteriorhodopsins (bRs) in a lipid bilayer was studied using a binary hard–disk model. The phase diagrams were calculated, using two-dimensional free volume theory. The critical concentrations of the bR ordering for the monomers and the trimers were obtained from the phase diagrams. The critical concentration ratio agreed well with the experiment when the repulsive core interaction between the depletants, namely the lipids, was taken into account. The results suggest that the depletion effect is dominant for the bRs ordering. Results in this chapter are reproduced from [46], with the permission of AIP Publishing

2.1 Introduction

There is no attractive force between two hard spheres in a vaccum. However, an effective attraction between them may appear when other compounds are added. This phenomenon was formulated in 1954 by Asakura and Oosawa to discuss the effective interaction between two macromolecules in a dilute polymer solution [**?**, 7]. Under the dilute condition, the effective interaction of the Asakura–Oosawa (AO) theory is very accurate. This effective attractive interaction is driven by an entropy difference when the system is described by a canonical ensemble. In the 1970s, Vrij resumed the theoretical work on depletion interactions [9]. After the rediscovery, researchers applied the idea of depletion interaction to the crowding phenomena in a living cell [47–54]. They studied the depletion effects in the cell because various macromolecules are present in the cytoplasm at high concentrations (approx. 0.3 g/ml).

Concepts of the AO theory is not only valid for three-dimensional systems but also for two-dimensional system. Therefore, similarly to the 3D system, phase transitions mediated by depletion effects are expected in a 2D system [55]. However, according to the literature [33–35, 37, 39, 40], the phase transitions occur in different manners between 2D and 3D systems. In 2011, Bernard and Krauth performed simulations and showed that there is a hexatic phase between the fluid and solid phases in the 2D hard disk one component system [37]. The details are explained in the chapter??. Recently, simulations of two-component hard–disk systems were carried out. The results showed that the hexatic phase of the larger disks disappeared when the size ratio was $1 : 1.4$ and the packing fraction of the smaller disk was large [36]. Therefore, the fluid–solid phase transition is expected due to the depletion effects in the binary hard disk systems.

In this thesis, I consider biological membranes, namely lipid molecules–Bacteriorhodopsin two component system, and discuss the adoption of a simple model. In 3D systems, hard–sphere model have often been used as simple models to quantify the essential

physical properties. [15,56–59] The usefulness of the simple model can be understood in terms of the van der Waals picture. The details are explained in the section??. According to the van der Waals picture, the short-ranged repulsive interactions, namely molecular shapes, play a primary role in intermolecular correlations, and the direct intermolecular attraction plays a minor role [27]. In other words, the packing of the molecules is important to understand the effective interaction between molecules in a liquid. This picture has been confirmed, and it gives fruitful interpretations of the liquid structure [27–29] and the phase transition [60, 61]. The picture is valid for the condensed system with no hydrogen bond or no ion bond [27].

The membrane can be regarded as a 2D phase condensed by proteins and lipid molecules in the water. That is, the translational motions of proteins and lipid molecules are virtually constrained within the membrane, and each molecular axis is almost fixed. Therefore, I thought that the 2D packing problem should provide a new approach to the interpretation of biomembrane phenomena, although the molecular interactions are complex. The top view of bRs and lipid molecules looks like a disk. Hence, I examine the two-component hard–disk system as a model of the membrane because the arrangement of these molecules can be modeled in 2D.

The bacteriorhodopsin (bR) is a kind of trans-membrane protein. Wild-type bRs make trimers and they form a 2D ordering structure in a lipid bilayer [1, 2]. The bR ordering structure, called purple membranes, work as proton pumps in *Halobacterium salinarum*. Some kinds of mutant bRs were reported to construct the 2D ordering structure, although they did not form trimers [43]. The critical concentrations (CC) of the mutant bRs for 'crystallization' are much larger than those of the wild-type bRs [45]. The ratio of the monomer-CC to the trimer-CC (CCR) is about 10.2 [45]. The details are in section??

The driving force for the ordering of the bRs has not yet been clarified. There is no covalent bond, hydrogen bond, or ionic bond between bRs in the membrane [41]. On the other hand, lateral depletion interactions between the bRs are expected [7, 9]. Basically, the lipid molecules and the bRs are confined to the lipid bilayer. The pseudo-2D space is crowded by the lipid molecules and the proteins. Therefore, in this thesis, the depletion interaction caused by the lateral translational motion of lipid molecules was studied.

2.2 Binary hard disk model and two-dimensional free volume theory

Because the exposure of the bRs and the lipid molecules to an aqueous phase must pay large penalties in free energy, the motions of these molecules are confined to the psudo-2D space. Hence, the 2D binary hard–disk model was adopted (FIG.2.1). The diameter $\sigma_{\rm tri} = 6.2$ nm for the bR trimer was estimated from an electron microscope image [1, 2, 62]. The estimated monomer diameter was about 3.0 nm. Three monomer diameters $\sigma_{\rm mono} = 2.9, 3.0,$ and 3.1 nm were examined to remove the arbitrariness for the model. The small disks were lipid molecules with the diameter $\sigma_{\rm lip} \sim 0.5$ nm [30]. For the same reason, three diameters $\sigma_{\rm lip} = 0.4, 0.5,$ and 0.6 nm were examined.

The isothermal system, consisting of the binary hard–disks, contacts with a reservoir that contains only small disks (lipid molecules). The system is in osmotic equilibrium with the reservoir. The depletion effect in the system is controlled by the packing fraction of small disks in the reservoir. The coexistence curves of the bR fluid and the ordered phases were obtained by two equations, as follows:

$$p_{\rm f}\left(\eta_{\rm bR}^{\rm fluid}, \eta_{\rm lip}^{\rm res}\right) = p_{\rm ord}\left(\eta_{\rm bR}^{\rm ordered}, \eta_{\rm lip}^{\rm res}\right), \tag{2.1}$$

$$\mu_{\rm f}\left(\eta_{\rm bR}^{\rm fluid}, \eta_{\rm lip}^{\rm res}\right) = \mu_{\rm ord}\left(\eta_{\rm bR}^{\rm ordered}, \eta_{\rm lip}^{\rm res}\right), \tag{2.2}$$

where $p_{\rm f}$ and $p_{\rm ord}$ are the bR pressures for the fluid and ordered phases, $\eta_{\rm bR}^{\rm fluid}$ and

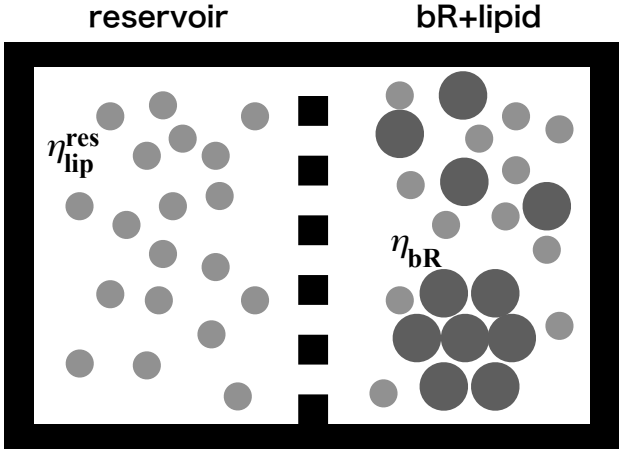

Figure 2.1: The binary hard–disk system (right side) with a reservoir of small disks (left side). The bRs and the lipid molecules are modeled as larger and smaller disks, respectively. The packing fraction of lipid molecules η_{lip} in the binary hard–disk system is controlled by $\eta_{\mathrm{lip}}^{\mathrm{res}}$ and η_{bR}.

$\eta_{\mathrm{bR}}^{\mathrm{ordered}}$ are the bR packing fractions for the fluid and ordered phases, $\eta_{\mathrm{lip}}^{\mathrm{res}}$ is the packing fraction of lipid for the reservoir, and μ_{f}, and μ_{ord} are the bR chemical potentials for the fluid and ordered phases, respectively. Therefore, the values for $p_{\mathrm{f}}(\eta_{\mathrm{bR}}^{\mathrm{fluid}}, \eta_{\mathrm{lip}}^{\mathrm{res}})$, $p_{\mathrm{ord}}(\eta_{\mathrm{bR}}^{\mathrm{ordered}}, \eta_{\mathrm{lip}}^{\mathrm{res}})$, $\mu_{\mathrm{f}}(\eta_{\mathrm{bR}}^{\mathrm{fluid}}, \eta_{\mathrm{lip}}^{\mathrm{res}})$, and $\mu_{\mathrm{ord}}(\eta_{\mathrm{bR}}^{\mathrm{ordered}}, \eta_{\mathrm{lip}}^{\mathrm{res}})$ were calculated. Basically, the method was similar to that explained in a textbook [14, 24]. While the textbook describes 3D systems, the present system is 2D. Not only the 2D Carnahan-Staring-like equation of state (2D–CSE) [63] was examined, but also the 2D scaled particle theory (2D–SPT) [23, 64] for the pure bR fluid phases.

First, the pressure and the chemical potential of the pure bR system for the fluid and the ordered phase were obtained. The pressure of pure bRs for the fluid phase p_{f}^0 is obtained by 2D–CSE as follows:

$$\beta p_{\mathrm{f}}^0 v_{\mathrm{bR}} = \frac{\eta_{\mathrm{bR}} + (\eta_{\mathrm{bR}})^2/8}{(1-\eta_{\mathrm{bR}})^2}, \tag{2.3}$$

where η_{bR}, β, and v_{bR} are the packing fractions of the bRs, $1/(\mathrm{k_B}T)$, and the area for a bR, respectively; $\mathrm{k_B}$ is the Boltzmann constant and T is the absolute temperature. The chemical potential of pure bRs for the fluid phase μ_{f}^0 is obtained using Gibbs-Duhem relation as

$$\begin{aligned}\beta\mu_{\mathrm{f}}^0 = \ln\left[\frac{\Lambda^2}{v_{\mathrm{bR}}}\right] + \ln[\eta_{\mathrm{bR}}] - \frac{7}{8}\ln[1-\eta_{\mathrm{bR}}] \\ + \frac{7}{8(1-\eta_{\mathrm{bR}})} + \frac{9}{8(1-\eta_{\mathrm{bR}})^2} - 2,\end{aligned} \tag{2.4}$$

where $\Lambda = \mathrm{h}(2\pi m_{\mathrm{bR}}\mathrm{k_B}T)^{-1/2}$ is the thermal de Broglie wavelength in the 2D space. h and m_{bR} are the Planck constant and the mass for one bR, respectively. By using 2D–SPT, p_{f}^0 and μ_{f}^0 were also obtained, as follows:

$$\beta p_{\mathrm{f}}^{0} v_{\mathrm{bR}} = \frac{\eta_{\mathrm{bR}}}{\left(1-\eta_{\mathrm{bR}}\right)^{2}}, \tag{2.5}$$

$$\beta \mu_{\mathrm{f}}^{0} = \ln\left[\frac{\Lambda^{2}}{v_{\mathrm{bR}}}\right] + \ln\left[\frac{\eta_{\mathrm{bR}}}{1-\eta_{\mathrm{bR}}}\right] + \frac{2-\eta_{\mathrm{bR}}}{\left(1-\eta_{\mathrm{bR}}\right)^{2}} - 2. \tag{2.6}$$

The derivation is shown in Appendix B.2

By contrast, the pressure and the chemical potential of the 2D crystal of pure bRs were substituted with the values of the 2D-ordered state. The cell theory for a 2D system [65] was adopted for this calculation. The pressure and chemical potential for the hexagonal lattice are

$$\beta p_{\mathrm{ord}}^{0} v_{\mathrm{bR}} = \frac{2\eta_{\mathrm{bR}}}{1-\eta_{\mathrm{bR}}/\eta_{\mathrm{cp}}}, \tag{2.7}$$

$$\beta \mu_{\mathrm{ord}}^{0} = \ln\left[\frac{\Lambda^{2}}{v_{\mathrm{bR}}}\right] - 2\ln\left[\frac{\eta_{\mathrm{cp}}}{\eta_{\mathrm{bR}}} - 1\right] + \frac{2\eta_{\mathrm{cp}}}{\eta_{\mathrm{cp}}-\eta_{\mathrm{bR}}}, \tag{2.8}$$

where $\eta_{\mathrm{cp}} = \pi/2\sqrt{3}$ is the packing fraction at close packing.

The adoption of the hexagonal lattice as the ordered phase is discussed here. The first problem is the possibility of existence of a long-range positional order. Theoretical studies, such as the Mermin-Wagner theorem, seemed to rule out the existence of an infinite long-range positional order [39, 40]. By contrast, a 2D hexagonal bR ordering structure has been observed experimentally on the purple membrane of the bacteria [1,2]. The diameter of the ordering structure is large, but is not infinite. It is at most 0.5 μm and the patch has about 6000 bR trimers [66]. It seems that the finite ordering structure is stable in the bacteria. I think that this ordered state can be treated approximately as a crystal.

The second problem is the validity for ignoring hexatic phase. A hexatic phase appears near the solid phase in one component's hard–disc system [33–35, 37]. It means that the hexatic phase is most stable in the region. The fragility of the hexatic phase was shown in a simulation study [36]. According to the study of a binary mixture of hard–disks, the hexatic phase shrinks and disappears as the number of small disks increases in the binary system. The shrinking appears at very low concentrations of the small disk. In this chapter, the behaviors of the binary system is discussed at the medium and high concentrations of the small disk, i.e., the lipid molecule. Therefore, the hexagonal lattice was adopted as the ordered state. The semi-grand potential $\Omega\left(N_{\mathrm{bR}}, V, T, \mu_{\mathrm{lip}}\right)$ is obtained by two-dimensional free volume theory (2D–FVT) as follows:

$$\Omega\left(N_{\mathrm{bR}}, V, T, \mu_{\mathrm{lip}}\right) = F^{0}\left(N_{\mathrm{bR}}, V, T\right) - p^{\mathrm{res}}\left\langle V_{\mathrm{free}}^{\mathrm{mix}}\right\rangle. \tag{2.9}$$

Here, F^{0} is the Helmholtz free-energy of a bR-pure system, $p^{\mathrm{res}}$is the pressure of the reservoir system, and $\left\langle V_{\mathrm{free}}^{\mathrm{mix}}\right\rangle$ is the free-area of lipid in the lipid–bR system. The derivation is shown in Appendix A. An approximation [24] is adopted to replace $\left\langle V_{\mathrm{free}}^{\mathrm{mix}}\right\rangle$ by the free volume in the pure bR system $\left\langle V_{\mathrm{free}}^{\mathrm{mix}}\right\rangle_{0}$. The pressure of ideal gas ($p_{\mathrm{IG}}^{\mathrm{res}}$) or 2D–SPT ($p_{\mathrm{SPT}}^{\mathrm{res}}$) and p^{res} are as follows:

$$\beta p_{\mathrm{IG}}^{\mathrm{res}} v_{\mathrm{bR}} = \frac{N_{\mathrm{lip}}^{\mathrm{res}} v_{\mathrm{lip}} q^{-2}}{V^{\mathrm{res}}} = \eta_{\mathrm{lip}}^{\mathrm{res}} q^{-2}, \tag{2.10}$$

$$\beta p_{\mathrm{SPT}}^{\mathrm{res}} v_{\mathrm{bR}} = \frac{\eta_{\mathrm{lip}}^{\mathrm{res}} q^{-2}}{\left(1-\eta_{\mathrm{lip}}^{\mathrm{res}}\right)^{2}}. \tag{2.11}$$

Here, v_{lip} is the area of a lipid molecule, $N_{\mathrm{lip}}^{\mathrm{res}}$ is the number of lipid molecules in the reservoir system, V^{res} is the area of reservoir system, and q is the diameter ratio between a bR (monomer or trimer) and a lipid molecule. The $\left\langle V_{\mathrm{free}}^{\mathrm{mix}}\right\rangle_0$ is obtained using the scaled particle theory as follows:

$$\left\langle V_{\mathrm{free}}^{\mathrm{mix}}\right\rangle_0 = V^{\mathrm{mix}}\alpha. \tag{2.12}$$

Here, α is defined as

$$\alpha \equiv \exp\left[-\beta W\right], \tag{2.13}$$

V^{mix} is the area of the lipid–bR system, and W is the work to insert a lipid molecule in the bR-pure system. α is calculated using 2D–SPT as follows:

$$\alpha = (1-\eta_{\mathrm{bR}})\exp\left[-\frac{2\eta_{\mathrm{bR}}q}{1-\eta_{\mathrm{bR}}} - \frac{q^2\eta_{\mathrm{bR}}}{(1-\eta_{\mathrm{bR}})^2}\right]. \tag{2.14}$$

The derivation is shown in Appendix B.1.

The pressure and chemical potential are obtained from $\Omega\left(N_{\mathrm{bR}}, V, T, \mu_{\mathrm{lip}}\right)$, as follows:

$$p = p^0 + p^{\mathrm{res}}\alpha - p^{\mathrm{res}}\eta_{\mathrm{bR}}\left(\frac{\partial\alpha}{\partial\eta_{\mathrm{bR}}}\right)_{N_{\mathrm{bR}},T,\mu_{\mathrm{lip}}}, \tag{2.15}$$

$$\mu_{\mathrm{bR}} = \mu_{\mathrm{bR}}^0 - p^{\mathrm{res}}v_{\mathrm{bR}}\left(\frac{\partial\alpha}{\partial\eta_{\mathrm{bR}}}\right)_{V,T,\mu_{\mathrm{lip}}}, \tag{2.16}$$

$$\begin{aligned}\left(\frac{\partial\alpha}{\partial\eta_{\mathrm{bR}}}\right) =& \frac{-\eta_{\mathrm{bR}}^2 + (-q^2+2q+2)\eta_{\mathrm{bR}} - q^2 - 2q - 1}{(1-\eta_{\mathrm{bR}})^2} \\ & \exp\left[-\frac{2\eta_{\mathrm{bR}}q}{1-\eta_{\mathrm{bR}}} - \frac{\eta_{\mathrm{bR}}q^2}{(1-\eta_{\mathrm{bR}})^2}\right],\end{aligned} \tag{2.17}$$

where $p^0$and μ_{bR}^0 are pressure and chemical potential in the bR-pure system.

2.3 Phase diagrams obtained by two-dimensional free volume theory

The free energies of pure bR-ordered and pure fluid phases were calculated by using cell theory and 2D–CSE, respectively. p^{res} is substituted by $p_{\mathrm{SPT}}^{\mathrm{res}}$. In other words, the lipid molecules were modeled as hard disks in the reservoir. The phase diagrams for the bR trimers (solid) and bR monomers (dots) are shown in FIG. 2.2(a). The y axis shows the packing fraction of lipid molecules in the reservoir and the x axis shows that of bRs. In the case of the pure bR system ($\eta_{\mathrm{lip}}^{\mathrm{res}} = 0$), the region $0.703 < \eta_{\mathrm{bR}} < 0.747$ is the coexistence region (fluid + ordered state).

The coexistence regions of the bRs expand around $\eta_{\mathrm{lip}}^{\mathrm{res}} = 0.35$. This expansion appears both boundary of the fluid side and ordered state side. The fluid side boundary decreases monotonically as $\eta_{\mathrm{lip}}^{\mathrm{res}}$ increases and there is no critical point. The coexistence region for the bR trimer ($q = 0.08065$) is wider than that for the bR monomer ($q = 0.16667$). In other words, as the parameter q decreases, the coexistence region becomes wider. This q-dependence of the width for the coexistence region is consistent with the q-dependence of the effective attraction between large disks. The q-dependence of the effective attraction is discussed using second virial coefficients in chapter 3.4.

The bR-ordered phase appears at the boundary of the fluid side, and the concentration at the boundary is the CC for the ordered phase. The CC value of the trimers is lower than that of the monomers. For example, when the $\eta_{\mathrm{lip}}^{\mathrm{res}}$ was 0.4, the CC for the trimers

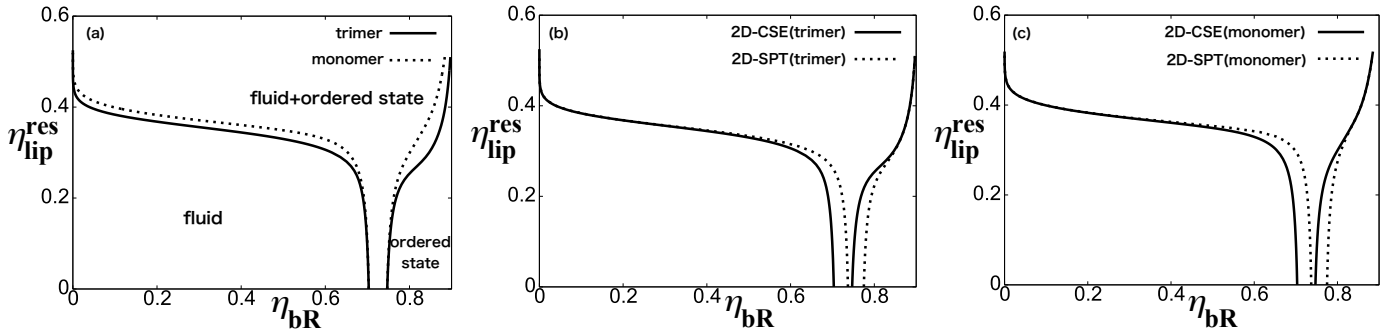

Figure 2.2: Phase diagrams of two-component hard–disk systems. $q = 0.16667$ (monomer-lipid system), $q = 0.08065$ (trimer-lipid system). (a) Phase diagrams of the bR trimer (solid curves) and the bR monomer (dotted curves). The free energy of pure bR fluid was calculated on the basis of 2D–CSE. (b) Phase diagrams of the bR trimer. The free energy of pure bR fluid was calculated on the basis of 2D–CSE (solid curves) and 2D–SPT (dotted curves). (c) Phase diagrams of the bR monomer. The free energy of pure bR fluid was calculated on the basis of 2D–CSE (solid curves) and 2D–SPT (dotted curves).

was 0.042 and that for the monomer 0.100. The CC difference obtained from the phase diagrams qualitatively agrees with that obtained by the experiments [45].

When the $\eta_{\rm lip}^{\rm res}$ is larger than 0.35, the fluid side boundary is shifted to the very low packing fraction $\eta_{\rm bR}$, as mentioned above. This shift is explained based on the depletion effects induced by the lateral translational motion of lipid molecules, as follows. The depletion forces between bRs become stronger with increasing the packing fraction of the lipid molecules. This effective attraction causes the sudden boundary shift around $\eta_{\rm lip}^{\rm res} = 0.35$ [7, 9].

In this 2D system, the high–low density fluids coexistence region, i. e. vapor–liquid coexistence region, does not exist because the critical point is not exist. It means that the bR disordered 2D condensed phase is not observed on the membrane. In FIG. 2.2(a), 2D–CSE was adopted to obtain the free energy for the reference fluid phase; namely, the pure bR fluid phase. Another theory, namely 2D–SPT, was adopted for comparison. The free energy for the reference ordered phase was calculated by the cell theory, again. The theory and connection of the reservoir are also similar to the calculation for FIG. 2.2(a). The phase diagrams are shown in FIG. 2.2(b) and (c) to compare with those given by the 2D–CSE and 2D–SPT.

For the pure bR system ($\eta_{\rm lip}^{\rm res} = 0$) the coexistence region calculated by using 2D–SPT was $0.737 < \eta_{\rm bR} < 0.775$. The coexistence region calculated by using 2D–SPT is a higher $\eta_{\rm bR}$ than that calculated by using 2D–CSE. This difference was caused by the difference between 2D–CSE and 2D–SPT, because there was no depletant in this system. On the other hand, the depletion effect becomes stronger as the $\eta_{\rm lip}^{\rm res}$ increases.

As the $\eta_{\rm lip}^{\rm res}$ increases, the difference between phase diagrams based on 2D–SPT and 2D–CSE disappears. When the $\eta_{\rm lip}^{\rm res} > 0.35$, the coexistence regions overlap in FIG. 2.2(b) and (c). This overlap indicates that the depletion effects become more dominant for bR ordering than the reference system as the depletion effect induced by lipid molecules increases. That is, when the $\eta_{\rm lip}^{\rm res}$ is above 0.35, the depletion force almost determines the CC for bR ordering. Therefore, it seems that the difference between the theories of the reference system disappears.

Some results for the 2D one-component hard–disk system are brought here from references [37, 67] to discuss the present results. According to the simulation study, the boundary between the fluid and the coexistence regions exists at 0.700 [37]. An exper-

imental study gives the value 0.68 for the boundary [67]. The fluid phases disappear at 0.716 (simulation) [37] and 0.70 (experiment) [67]. The fluid and hexatic phases disappear when the packing fraction increases. The monophase for solid becomes most stable under the high packing fraction region. The boundary between the hexatic and solid phases is 0.720 (simulation) and 0.73 (experiment), respectively [37, 67].

In the present study, the hexagonal crystal structure was adopted as the ordered phase, and the coexistence regions for the fluid–ordered phase appear $0.703 - -0.747$ (for 2D–CSE and 2D–FVT) and $0.737 - -0.775$ (for 2D–SPT and 2D–FVT). These values are different from the exact values given by the simulations and the experiments. This reason seems to be that the free energy for the hexagonal lattice structure is different from that for the hexatic phase. However, it does not mean that the present results are meaningless to obtain the CCR. Because of the depletion effect, these differences on the boundaries disappear at the packing fraction of the bio-membrane ($\eta_{\rm lip}^{\rm res} = 0.5$) [30]. FIG. 2.2(b) and (c) show that the CC boundaries virtually agree with each other in the region $\eta_{\rm lip}^{\rm res} > 0.38$, suggesting that the effective attraction is strong enough. I, therefore, assume that the argument of the hexatic phase for the reference bR system is avoided for the CCR in this thesis.

2.4 CCRs obtained using two-dimensional free volume theory

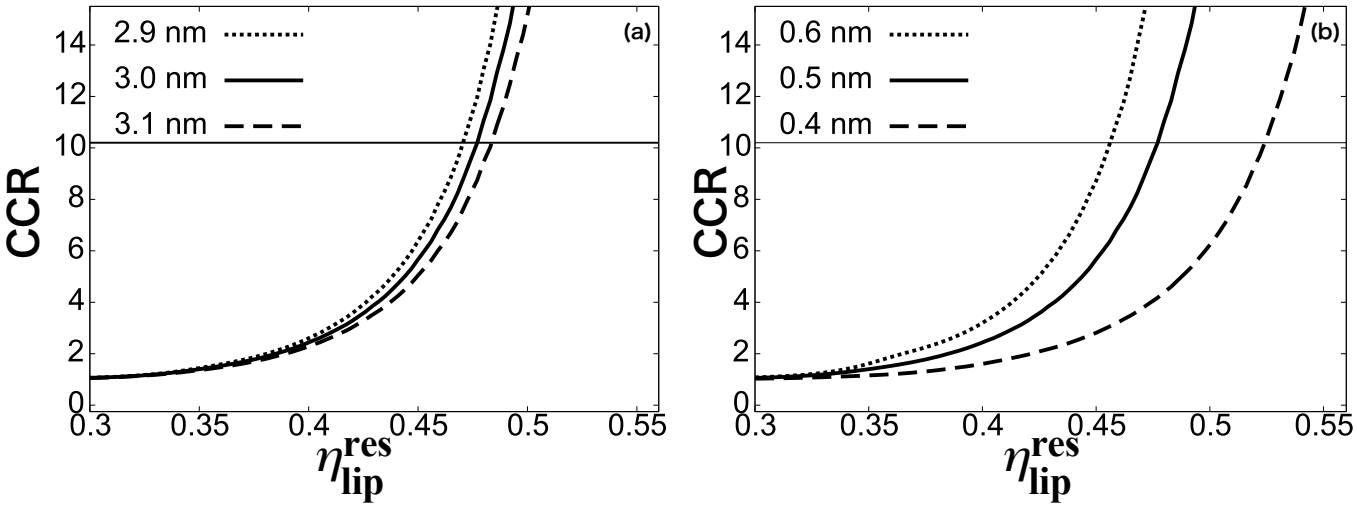

Figure 2.3: Calculated CCR of bR trimers to monomers. The horizontal thin solid line shows the experimental value, 10.2. (a) The diameter of the lipid molecule is 0.5 nm. The dotted curve (bR monomer diameter: 2.9 nm), the solid curve (bR monomer diameter: 3.0 nm), the dashed curve (bR monomer diameter: 3.1 nm). (b) The diameter of bR monomer is 3.0 nm. The dotted curve (the lipid diameter: 0.6 nm), solid curve (the lipid diameter: 0.5 nm), dashed curve (the lipid diameter: 0.4 nm).

CCRs (CC for monomer/CC for trimer) were obtained to compare between the calculated and experimental results. CCR becomes larger than 1 because the CC for the bR trimer is lower than that for the bR monomer. The calculated CCR results are shown in FIG. 2.3(a) and (b). In all models, the CCRs monotonically increase as the $\eta_{\rm lip}^{\rm res}$ increases. The increase in CCR becomes steeper as the monomer diameter decreases (FIG. 2.3(a)). On the other hand, the increase in CCR becomes steeper as the lipid diameter increases (FIG. 2.3(b)). Hence, the CCR curves depend on the model. Here, 2.9 and 3.1 nm are small enough and large enough for the monomer size, respectively; 0.4 and 0.6 nm are also too small and too large for the lipid size, respectively. Therefore, the

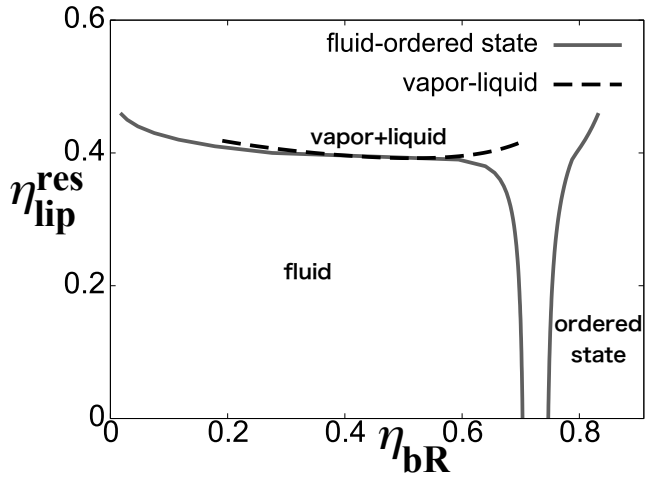

Figure 2.4: Phase diagram of the protein ($q = 0.27$). The solid curves show the coexistence region between the fluid and the ordered state. The dashed curve shows the coexistence region between vapor and liquid.

ranges for the parameters are wide enough to discuss the ordering mechanism.

The CCR experimental value is about 10.2 [45]. For example, when the diameters of the lipid molecule and the bR monomer are 0.5 nm and 3.0 nm, respectively, the calculated CCR agrees with the experimental CCR at the $\eta_{\mathrm{lip}}^{\mathrm{res}} = 0.477$. This result is important. According to literature [30], the lipid number density of a cell membrane monolayer is $2.5 \times 10^6 \mu\mathrm{m}^{-2}$. When the monomer diameter is 2.9, 3.0, and 3.1 nm, the calculated CCRs agree with the experimental CCR at the lipid number densities of $=$ 2.40, 2.43, and $2.46 \times 10^6 \mu\mathrm{m}^{-2}$, respectively. Each value is almost the same, about $2.4 \times 10^6 \mu\mathrm{m}^{-2}$. This value is reasonable compared with $2.5 \times 10^6 \mu\mathrm{m}^{-2}$.

When the lipid diameter is 0.4, 0.5, and 0.6 nm, the calculated CCR agrees with the experimental CCR at the lipid number densities of 4.17, 2.43, and $1.61 \times 10^6 \mu\mathrm{m}^{-2}$, respectively. The calculated results are reasonable because the calculated lipid number density of $2.43 \times 10^6 \mu\mathrm{m}^{-2}$ is very close to the estimated value of $2.5 \times 10^6 \mu\mathrm{m}^{-2}$ for a cell membrane monolayer. The orders of 4.17 and $1.61 \times 10^6 \mu\mathrm{m}^{-2}$ are also the same as that of $2.5 \times 10^6 \mu\mathrm{m}^{-2}$.

Calculated results suggest that the driving force for the ordering is the depletion effect. Although the model is simple, the calculated CCR is very close to the experimental value. Indeed, the calculated results depend on the size ratios between disks. However, the calculated results remain reasonable if the parameters for the models are chosen in realistic values. Therefore, it seems that this conclusion is robust.

2.5 Vaper–liquid phase transition

When the ordered state of the bR is discussed, the location of the vapor (large disk poor)–liquid (large disk rich) coexistence curve in the phase diagram should be taken into account. According to some papers, the vapor–liquid phase separation appears when q becomes larger [55,68]. Here, the value q is obtained when the critical point appears. I adopted $p_{\mathrm{SPT}}^{\mathrm{res}}$ for the pressure of the reservoir and the 2D–CSE for the reference system of the fluid phase. The vapor–liquid transition becomes stable when q is larger than 0.27. The phase diagram for $q = 0.27$ is shown in FIG. 2.4. In this case, the vapor–liquid coexistence curve almost overlaps the liquid–ordered state coexistence curve around the critical point. The value 0.27 is near as those values given by other methods [55, 68]. The discussion goes back to the ordered state of bR. Because 0.27 is much larger than

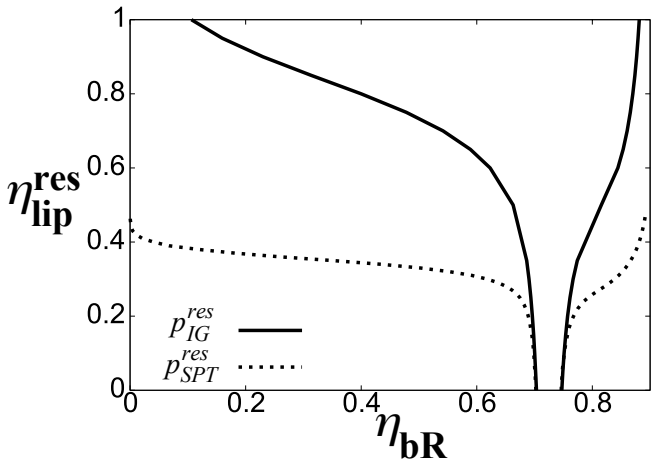

Figure 2.5: Phase diagrams of the protein ($q = 0.1$). The p^{res} was substituted by $p_{\mathrm{IG}}^{\mathrm{res}}$ (solid) and $p_{\mathrm{SPT}}^{\mathrm{res}}$ (dots).

0.16667 and 0.08065, it is expected that the vapor–liquid coexistence is not observed in the experiment.

Here, the calculated phase diagrams (FIG. 2.4) are compared with those reported in a paper [68]. As q increases, the critical point and the vapor–liquid coexistence region become clearer in the present study. This q dependence appears in the reference [68]. The critical point does not appear in the phase diagram for $q = 0.15$ in the reference [68], and the critical point appears in the phase diagram for $q = 0.3$, which means that the critical point appears somewhere from $q = 0.15$ to 0.3. In the paper, the phase diagrams are obtained using the density functional theory, a method different from the present study. In the other paper [55], the critical point is estimated to appear somewhere from $q = 0.3$ to 0.4. Although the details of the shape are slightly different from the diagrams in the present study, the q-dependence of the shape of the phase diagram is similar.

2.6 Phase diagrams and CCR using the ideal gas model in the reservoir

The lipid molecules in the reservoir were also modeled as ideal gas, and the phase diagrams were examined. The results showed another piece of information. The free energies for the reference system of the ordered state and of the fluid phase were obtained using 2D cell theory and 2D–CSE, respectively. The phase diagrams for $q = 0.1$ are shown in FIG. 2.5. The solid curves are the coexistence boundary with the ideal gas model for the reservoir. The dotted curves represent the coexistence boundary in the case of the hard disk reservoir where the pressure is obtained by 2D–SPT. The fluid side boundaries decrease monotonically as $\eta_{\mathrm{lip}}^{\mathrm{res}}$ increases and there is no critical point in both cases. The features are the same in both. However, the quantitative differences are remarkable. The coexistence region for the hard disk reservoir expands widely even when $\eta_{\mathrm{lip}}^{\mathrm{res}}$ is low. By contrast, the coexistence region for the ideal gas reservoir is much narrower than that for the hard disk reservoir. The coexistence region for the ideal gas reservoir expands around $\eta_{\mathrm{lip}}^{\mathrm{res}} = 0.6$ whereas that for the hard disk reservoir expands around $\eta_{\mathrm{lip}}^{\mathrm{res}} = 0.35$. The packing fraction of lipid molecules in a biomembrane is about 0.5 in the case of $\sigma_{\mathrm{lip}} = 0.5$ nm [30]. These results suggest that the depletion effects could hardly work in a biomembrane if the collisions between lipid molecules are ignored.

The phase diagrams of bRs are also calculated assuming an ideal gas reservoir. The

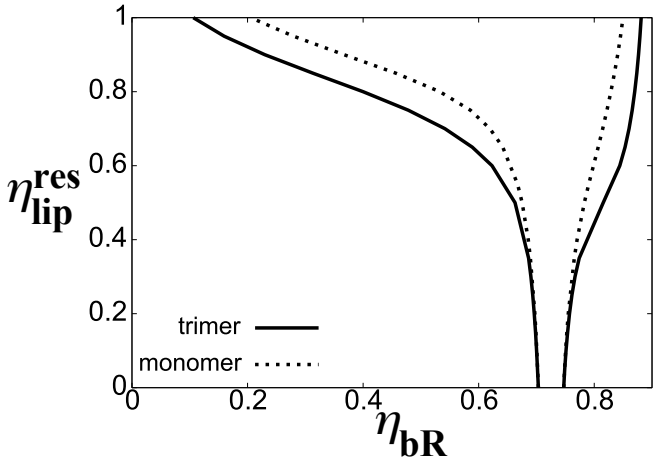

Figure 2.6: Phase diagrams of the bR trimer (solid curves, $q = 0.08065$) and the bR monomer (dotted curves, $q = 0.16667$). The ideal gas model was adopted as the lipid reservoir.

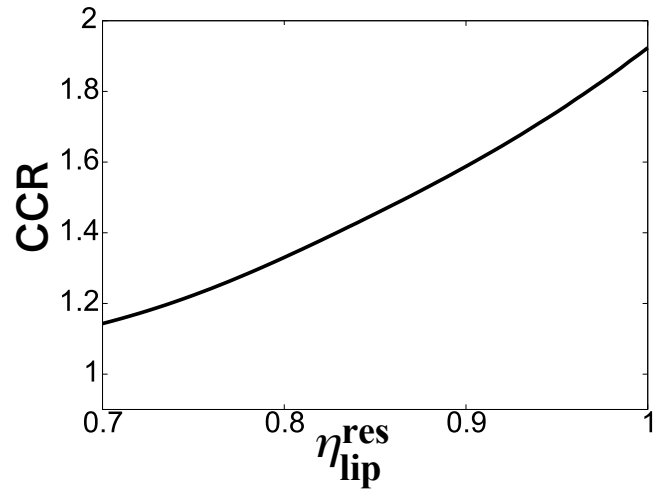

Figure 2.7: Calculated CCR of bR trimers to monomers. q for the bR trimer and monomer is 0.08065 and 0.16667, respectively. The ideal gas model was adopted as the lipid reservoir.

phase diagrams for the bR trimers (solid) and the bR monomers (dots) are shown in FIG. 2.6. Even when the reservoir is the ideal gas model, the coexistence region for the bR trimer (q = 0.08065) is wider than that for the bR monomer (q = 0.16667). For example, when the $\eta_{\mathrm{lip}}^{\mathrm{res}}$ is 0.7, the CC for the trimers is 0.542 and that for the monomer 0.620. The calculated large/small relation of CCs qualitatively again agrees with that obtained by the experiments [45]. However, the results have serious quantitative problems. CCs are too large when the $\eta_{\mathrm{lip}}^{\mathrm{res}}$ is about 0.5. The CCs for trimers and monomers are 0.663 and 0.675, respectively. The ratio is about 1. If a reasonable value for CCR (about 10) is assumed, the packing fraction $\eta_{\mathrm{lip}}^{\mathrm{res}}$ could become an unrealistic value. The calculated CCR for the ideal gas reservoir is shown in FIG. 2.7. qs for the trimer and monomer are 0.08065 and 0.16667. The CCR is 1.608 even when the reservoir packing fraction is the closest ($\eta_{\text{closest packing}} = \pi/(2\sqrt{3}) \sim 0.907$). By contrast, the CCRs are reasonable when the hard disk model is adopted as the lipid reservoir. Therefore, the granularity of the lipid molecule is important for the lateral depletion effects on the bR ordering.

The numerical disagreement between the results for the hard disk reservoir and for

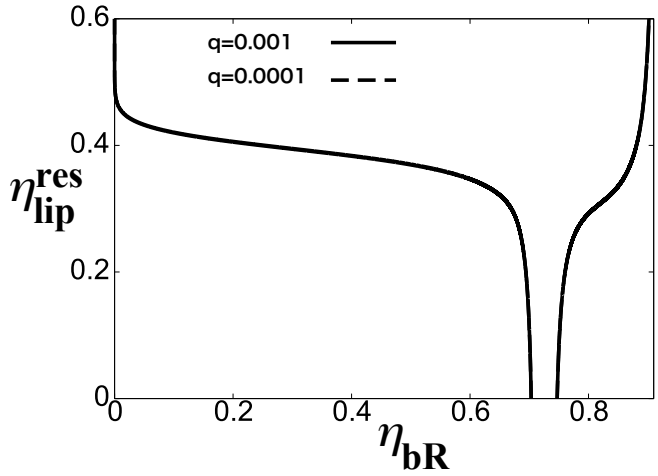

Figure 2.8: The phase diagrams for small qs calculated by the 2D–FVT approach. The solid and dashed curves show the phase diagrams for q =0.001 and 0.0001, respectively. These coexistence regions almost overlap each other.

the ideal gas reservoir is remarkable. The disagreement is discussed based on the equations of state. The equations of state for 2D–SPT and 2D–CSE show that the pressures are much higher than for the ideal gas because each lipid molecule has a repulsive core, and they are crowded in the reservoir. There is a positive correlation between the pressure in the reservoir and the depletion force. Thus, the effective attraction between bRs becomes stronger than for the ideal gas reservoir. Therefore, the results indicate that the crowding in the reservoir is important in the calculation of the depletion effects.

2.7 Problem of two-dimensional free volume theory

Results calculated using the 2D–FVT show good agreement with experimental results. However, there is problem for the FVT when q is very small. García et al. reported that the q-dependence of the phase diagram obtained by the FVT disappears in a 3D system as the value q decreases [69]. They further noticed that this result did not agree with an experimental result qualitatively [69]. This problem in the 3D systems should be conserved in the 2D systems. Thus, the q-dependence of phase diagrams obtained using the 2D–FVT was examined. FIG.2.8 shows the phase diagrams for $q = 0.001$ and 0.0001 calculated using the 2D–FVT approach. These coexistence regions almost overlap each other. This agreement numerically shows that the theoretical approach does not have q dependence when q is small.

The disappearance of the q-dependence for the 2D–FVT approach at small q has to be explained. In the phase diagram calculation, the bR packing fraction for the fluid phase $\eta_{\mathrm{bR}}^{\mathrm{fluid}}$ and that for the ordered phase, $\eta_{\mathrm{bR}}^{\mathrm{ordered}}$, must be obtained. These values are obtained by solving the equations (2.1) and (2.2) [24,46]. The pressure and the chemical

potential are expressed by 2D–FVT [24, 46], as follows:

$$\beta p_{\rm f} v_{\rm bR} = \beta p_{\rm f}^0 v_{\rm bR} + \beta p^{\rm res} v_{\rm bR} \left(\alpha_{\rm f} - \eta_{\rm bR}^{\rm fluid} \left(\frac{\partial \alpha_{\rm f}}{\partial \eta_{\rm bR}^{\rm fluid}} \right)_{N_{\rm bR},T,\mu_{\rm lip}} \right), \tag{2.18}$$

$$\beta p_{\rm ord} v_{\rm bR} = \beta p_{\rm ord}^0 v_{\rm bR} + \beta p^{\rm res} v_{\rm bR} \left(\alpha_{\rm ord} - \eta_{\rm bR}^{\rm ordered} \left(\frac{\partial \alpha_{\rm ord}}{\partial \eta_{\rm bR}^{\rm ordered}} \right)_{N_{\rm bR},T,\mu_{\rm lip}} \right), \tag{2.19}$$

$$\beta \mu_{\rm f,bR} = \beta \mu_{\rm f,bR}^0 - \beta p^{\rm res} v_{\rm bR} \left(\frac{\partial \alpha_{\rm f}}{\partial \eta_{\rm bR}^{\rm fluid}} \right)_{V,T,\mu_{\rm lip}}, \tag{2.20}$$

$$\beta \mu_{\rm ord,bR} = \beta \mu_{\rm ord,bR}^0 - \beta p^{\rm res} v_{\rm bR} \left(\frac{\partial \alpha_{\rm ord}}{\partial \eta_{\rm bR}^{\rm ordered}} \right)_{V,T,\mu_{\rm lip}}, \tag{2.21}$$

where $\alpha_{\rm f}$ and $\alpha_{\rm ord}$ are the free volume fraction for the fluid phase and ordered phase, respectively. $p_{\rm f}^0$ and $p_{\rm ord}^0$ are the pressure for the fluid and ordered phases in a bR pure system. $\mu_{\rm f,bR}^0$ and $\mu_{\rm ord,bR}^0$ are the chemical potential for the fluid and ordered phases in the bR pure system. If these values are substituted to the relations (2.1) and (2.2), namely $p_{\rm f} = p_{\rm ord}$, $\mu_{\rm f,bR} = \mu_{\rm ord,bR}$, two equations are obtained, as follows:

$$\beta \left(p_{\rm f}^0 - \beta p_{\rm ord}^0 \right) v_{\rm bR} + \beta p^{\rm res} v_{\rm bR} \left(\alpha_{\rm f} - \eta_{\rm bR}^{\rm fluid} \left(\frac{\partial \alpha_{\rm f}}{\partial \eta_{\rm bR}^{\rm fluid}} \right) - \alpha_{\rm ord} + \eta_{\rm bR}^{\rm ordered} \left(\frac{\partial \alpha_{\rm ord}}{\partial \eta_{\rm bR}^{\rm ordrered}} \right) \right) = 0, \tag{2.22}$$

$$\beta \left(\mu_{\rm f,bR}^0 - \mu_{\rm ord,bR}^0 \right) - \beta p^{\rm res} v_{\rm bR} \left(\left(\frac{\partial \alpha_{\rm f}}{\partial \eta_{\rm bR}^{\rm fluid}} \right) - \left(\frac{\partial \alpha_{\rm ord}}{\partial \eta_{\rm bR}^{\rm ordered}} \right) \right) = 0. \tag{2.23}$$

$\alpha_{\rm f}$ and $\alpha_{\rm ord}$ are obtained by SPT [24, 46] as follows:

$$\alpha_{\rm f} = \left(1 - \eta_{\rm bR}^{\rm fluid}\right) \exp\left[-\frac{2\eta_{\rm bR}^{\rm fluid} q}{1 - \eta_{\rm bR}^{\rm fluid}} - \frac{\eta_{\rm bR}^{\rm fluid} q^2}{\left(1 - \eta_{\rm bR}^{\rm fluid}\right)^2} \right], \tag{2.24}$$

$$\alpha_{\rm ord} = \left(1 - \eta_{\rm bR}^{\rm ordered}\right) \exp\left[-\frac{2\eta_{\rm bR}^{\rm ordered} q}{1 - \eta_{\rm bR}^{\rm ordered}} - \frac{\eta_{\rm bR}^{\rm ordered} q^2}{\left(1 - \eta_{\rm bR}^{\rm ordered}\right)^2} \right]. \tag{2.25}$$

The partial differentiations are

$$\left(\frac{\partial \alpha_{\rm f}}{\partial \eta_{\rm bR}^{\rm fluid}} \right) = \frac{-(\eta_{\rm bR}^{\rm fluid})^2 + (-q^2 + 2q + 2)\eta_{\rm bR}^{\rm fluid} - q^2 - 2q - 1}{(1 - \eta_{\rm bR}^{\rm fluid})^2} \exp\left[-\frac{2\eta_{\rm bR}^{\rm fluid} q}{1 - \eta_{\rm bR}^{\rm fluid}} - \frac{\eta_{\rm bR}^{\rm fluid} q^2}{\left(1 - \eta_{\rm bR}^{\rm fluid}\right)^2} \right], \tag{2.26}$$

$$\left(\frac{\partial \alpha_{\rm ord}}{\partial \eta_{\rm bR}^{\rm ordered}} \right) = \frac{-(\eta_{\rm bR}^{\rm ordered})^2 + (-q^2 + 2q + 2)\eta_{\rm bR}^{\rm ordered} - q^2 - 2q - 1}{(1 - \eta_{\rm bR}^{\rm ordered})^2} \exp\left[-\frac{2\eta_{\rm bR}^{\rm ordered} q}{1 - \eta_{\rm bR}^{\rm ordered}} - \frac{\eta_{\rm bR}^{\rm ordered} q^2}{\left(1 - \eta_{\rm bR}^{\rm ordered}\right)^2} \right]. \tag{2.27}$$

The pressure in the reservoir is expressed using SPT [24, 46]: namely, eq. (2.11). The first term on the left-hand side in eqs. (2.22) and (2.23) does not depend on q. On the other hand, the behavior of the second term on the left-hand side in eq. (2.22) must be confirmed at the limit of $q = 0$ because the part $\beta p^{\rm res} v_{\rm bR}$ goes to infinity, and the

remaining part—namely, the part in the parentheses—goes to zero. The second term on the left-hand side in eq. (2.23) also has a similar problem. Thus, these second terms are expanded to polynomials to discuss the q-dependence.

The left-hand sides of eqs. (2.22) and (2.23) are expanded to the polynomial functions of q, as follows.

$$(p_{\rm f}^0 - p_{\rm ord}^0)v_{\rm bR} + \frac{\eta_{\rm lip}^{\rm res}}{(1-\eta_{\rm lip}^{\rm res})^2}\left(\frac{-\left(\eta_{\rm bR}^{\rm fluid}\right)^2}{(1-\eta_{\rm bR}^{\rm fluid})^2} + \frac{\left(\eta_{\rm bR}^{\rm ordered}\right)^2}{(1-\eta_{\rm bR}^{\rm ordered})^2}\right) + O(q) = 0 \qquad (2.28)$$

$$\mu_{\rm f}^0 - \mu_{\rm ord}^0 + \frac{\eta_{\rm lip}^{\rm res}}{(1-\eta_{\rm lip}^{\rm res})^2}\left(\frac{1-4\eta_{\rm bR}^{\rm fluid}+2\left(\eta_{\rm bR}^{\rm fluid}\right)^2}{(1-\eta_{\rm bR}^{\rm fluid})^2} - \frac{1-4\eta_{\rm bR}^{\rm ordered}+2\left(\eta_{\rm bR}^{\rm ordered}\right)^2}{(1-\eta_{\rm bR}^{\rm ordered})^2}\right) + O(q) = 0 \qquad (2.29)$$

The above two equations are solved to obtain the phase boundary. The $q-$dependence disappears at the limit of $q = 0$. Therefore, the phase diagram of the 2D–FVT approach does not depend on q for small q.

This disappearance of the q-dependence originates in $\alpha_{\rm f}$ and $\alpha_{\rm ord}$. The same theory, namely SPT, is used to express both $\alpha_{\rm f}$ and $\alpha_{\rm ord}$. Therefore, the 0th-order terms of q for the fluid and ordered phases cancel each other in eqs. (2.28) and (2.29). q for the bR trimer, 0.08065, is small. Therefore, this problem may affect the phase diagram. Thus, the CCRs should be examined by another approach.

2.8 Discussion

The disappearance of the q-dependence may affect the CC, namely CC for trimer. The 2D–FVT seems to underestimate the CC for the trimer because of the disappearance of the q-dependence. In other words, the 2D–FVT CC for the trimer seems to have larger value than the real CC due to the existence of lower limit of CC. Therefore, it can be predicted that the real CCRs increase more steeply as the lipid packing fraction increase. The effect of the problem is discussed comparing with CCRs obtaind using another theory, namely thermodynamic perturbation theory, in next chapter.

I also would like to discuss the validity of the assumption for the ordering structure. It is assumed that the ordered state for the pure bRs formed hexagonal lattice because it seemed that the argument of the hexatic phase could be avoided in the present study. According to a simulation study for the two-component disk, the hexatic phase disappears when the number ratio of the small disk is higher than 1% [36]. The result suggests that the smaller disks stabilize the hexagonal lattice structure of the larger disks. In the bio-membrane, the smaller disks, lipid molecules, are a major component and the fragile hexatic phase of bRs can be expected to disappear. On the other hand, the size ratio between disks q in the simulation (about 0.714) was much larger than in this study [36]. In those smaller qs, such as 0.08065 and 0.16667, the small disk could locate interstitially in the ordered large disks. And the system *in vivo* contain other molecules and the impurity effects are not clear. Therefore, further simulation studies are also needed.

2.9 Summary

In this chapter, the ordering behaviors of bR was discussed. The phase diagrams for the monomers and the trimers with lipid molecules were calculated by using 2D–FVT with a simple 2D model. The results showed that the depletion effect was dominant for the larger hard–disk ordering when the $\eta_{\rm lip}^{\rm res} > 0.35$. The calculated results for CCRs

agreed with the experimental results, suggesting that the depletion interactions induced by the lateral translational motions of lipid molecules drive the ordering of bRs, such as bRs. However, it was shown that the 2D–FVT had a problem when q was very small. Therefore, the CCRs should be examined by another approach.

Chapter 3

CCRs obtained using thermodynamic perturbation theory

Using binary hard disk mixture models, I studied the two-dimensional ordering of bacteriorhodopsins in a lipid bilayer. The phase diagrams were calculated using the thermodynamic perturbation theory. Two types of effective interactions were examined to discuss the lateral depletion effects caused by repulsive core interaction between lipid molecules. The results indicate that the core repulsions drastically broaden the coexistence region for the fluid–ordered phase, and the depletion force is the driving force for the bR crystallization.

3.1 Introduction

In the chapter 2, the phase diagrams obtained using 2D free volume theory (2D–FVT) suggested that the lateral depletion effect is dominant in the driving force of bR ordering. The study focused on the difference between the "crystallization" behaviors of wild-type bR and mutant bR, which construct the ordering structure. Although the mutant monomers do not construct trimers, they form a crystal [43]. The critical concentrations (CCs) of the mutant bRs for the "crystallization" are much larger than those of the wild-type bRs. According to experiments by M. P. Krebs et al., the ratio CCR$(=$ CC1$/$CC3$)$ is about 10.2, where CC1 and CC3 are the critical concentrations for the mutant monomers and the wild-type trimers, respectively [45].

The calculated results by using 2D–FVT also indicated that the depletion effect was too weak when the lipid molecules were modeled as an ideal gas, and it differed from the experimental result [46]. On the other hand, I also described the pressure of the reservoir using the two-dimensional scaled particle theory (2D–SPT) [23, 64], taking into account the effects of the repulsive core of the lipid molecule [46]. The phase diagrams were calculated based on the models. The calculated phase diagrams showed that the repulsive core enhanced the depletion effect, and the calculated CCRs virtually agreed with the experimental results [46]. Therefore, I discussed that the depletion effect significantly contributed to the "crystallization" in the chapter 2. However, the phase diagram calculated by using 2D–FVT is not correct when a diameter ratio between lipid and bR ($\sigma_{\mathrm{lip}}/\sigma_{\mathrm{bR}}$) is very small. Therefore, the CCR is examined by using another theory in this chapter.

In the chapter 2, the phase diagrams were obtained without calculating the effective interaction between bRs. In this chapter, first, I calculated the effective interactions between bR. Next, I calculated the free energies using the thermodynamic perturbation theory [70–72] with the effective interactions and obtained the phase diagrams. Finally, the phase diagrams gave the CCRs.

3.2 Model and theory

A binary hard-disk model was adopted in this chapter. The model is the same as that in the chapter 2. The lipid bilayer was regarded as a condensed 2D plane space. The lipid molecules, bR monomers, and bR trimers were modeled as small, medium, and large hard disks, respectively. The diameter for the bR trimer σ_{tri} was estimated as 6.2 nm [46,62]. The diameter for the bR monomer σ_{mono} was estimated as 3.0 nm [46]. The diameter for the lipid molecule $\sigma_{\mathrm{lip}}$was estimated as 0.5 nm [30,46]. In addition, the two lipid diameters $\sigma_{\mathrm{lip}} = 0.4$ and 0.6 nm were also examined to remove the arbitrariness for the model.

The system consisted of lipid and bR molecules. The binary hard-disk system was in osmotic equilibrium with a reservoir. Therefore, I obtained the effective interactions between bR molecules and calculated the phase diagrams using the effective one-component system. The effective interactions between bR molecules are explained as follows.

The AO and modified AO potentials [46] were adopted as the effective potential for bRs. The lipid molecules cannot enter the excluded area V_{ex} around the bR molecules in this model. The AO potential ω_{AO} between two bRs can be written as

$$\omega_{\mathrm{AO}}(r) = \infty, \quad r < \sigma_{\mathrm{bR}}, \tag{3.1}$$

$$\omega_{\mathrm{AO}}(r) = -\rho_{\mathrm{lip}}^{\mathrm{res}} \mathrm{k_B} T \Delta V_{\mathrm{ex}}(r), \quad r > \sigma_{\mathrm{bR}}, \tag{3.2}$$

where $\rho_{\mathrm{lip}}^{\mathrm{res}}$ is the number density of lipid molecules in the reservoir, $\mathrm{k_B}$ is Boltzmann constant, T is the absolute temperature, ΔV_{ex} is the overlap area of excluded volumes, r is the distance between the centers of bRs, and σ_{bR} is the diameter for bR. ΔV_{ex} is expressed analytically as follows,

$$\begin{aligned} \Delta V_{\mathrm{ex}}(r) = & \frac{1}{2}\sigma_{\mathrm{bR}}^2(1+q)^2 \arccos\left[\frac{r}{\sigma_{\mathrm{bR}}(1+q)}\right] \\ & -\frac{1}{4}\sigma_{\mathrm{bR}}^2(1+q)^2 \sin\left[2\arccos\left[\frac{r}{\sigma_{\mathrm{bR}}(1+q)}\right]\right], \end{aligned} \tag{3.3}$$

where q is the diameter ratio between the lipid molecule and bR ($\sigma_{\mathrm{lip}}/\sigma_{\mathrm{bR}}$). $\rho_{\mathrm{lip}}^{\mathrm{res}} \mathrm{k_B} T$ is regarded as the pressure of ideal gas in the reservoir. Therefore, the AO interaction is the pressure-area work for the two-dimensional ideal gas, and the area is ΔV_{ex} [24]. Thus, ω_{AO} also can be written as follows:

$$\omega_{\mathrm{AO}}(r) = \infty, \quad r < \sigma_{\mathrm{bR}}, \tag{3.4}$$

$$\omega_{\mathrm{AO}}(r) = -p^{\mathrm{res}} \Delta V_{\mathrm{ex}}(r), \quad r > \sigma_{\mathrm{bR}}. \tag{3.5}$$

In the conventional AO theory, the repulsive interactions between depletants are ignored, and the lipid molecules overlap. In other words, the pressure in the reservoir is that of the ideal gas. On the other hand, I replaced the pressure of the ideal gas reservoir with that estimated using the two-dimensional scaled particle theory (2D–SPT) [24,46], taking account of the repulsive interactions between depletants. Thus, the pressure in the reservoir was expressed as follows:

$$p^{\mathrm{res}} = \frac{\rho_{\mathrm{lip}}^{\mathrm{res}}}{\left(1-\eta_{\mathrm{lip}}^{\mathrm{res}}\right)^2} \mathrm{k_B} T, \tag{3.6}$$

where $\eta_{\mathrm{lip}}^{\mathrm{res}}$ is the reservoir's packing fraction of lipid molecules. Here, I call this the modified AO model. The modified AO potential ω_{Mod}, therefore, is written as

$$\omega_{\rm Mod}(r) = \infty, \ \ r < \sigma_{\rm bR}, \tag{3.7}$$

$$\omega_{\rm Mod}(r) = -\frac{\rho_{\rm lip}^{\rm res}}{\left(1-\eta_{\rm lip}^{\rm res}\right)^2} {\rm k_B} T \Delta V_{\rm ex}(r), \ \ r > \sigma_{\rm bR}. \tag{3.8}$$

In this model, there are only two bRs in the lipid condensed system. That is, a very low bR packing fraction was assumed in the system. As the bR packing fraction increases, the lipid packing fraction in the system decreases. Therefore, the effective interaction depends on the bR packing fraction. Here, I adopted an approximation that $\omega_{\rm Mod}$ is independent of the bR packing fraction [70, 71].

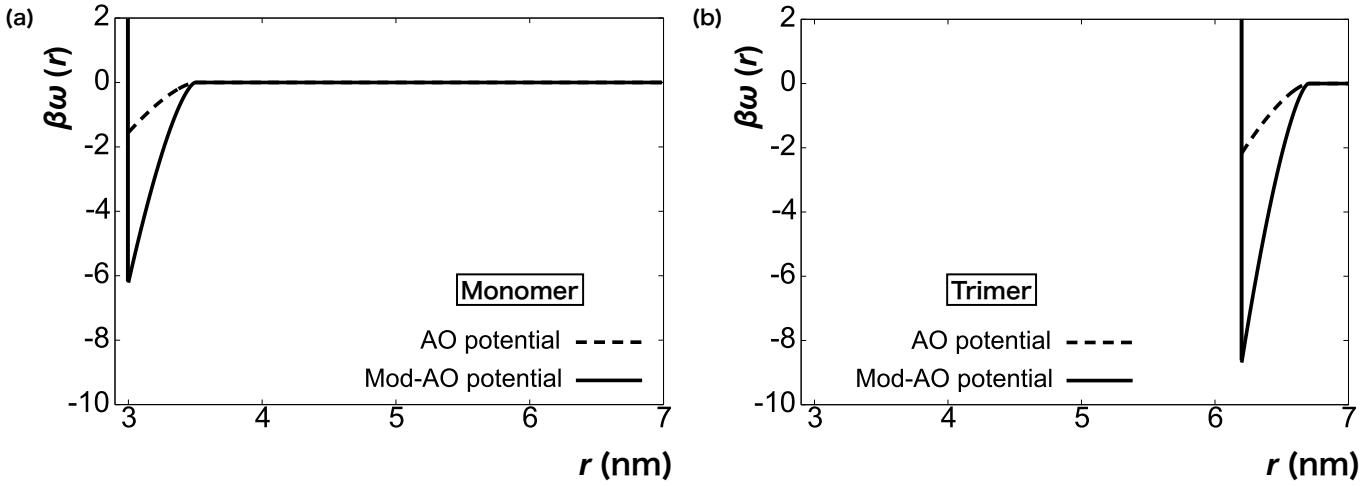

Figure 3.1: The effective potential between bR monomers (a) and trimers (b) at $\eta_{\rm lip}^{\rm res} = 0.5$. The lipid—bR diameter ratios, qs, are 0.16667 and 0.08065, respectively. The dashed curves show the AO potential. The solid curves show the modified AO potential.

FIG.3.1 shows the effective potentials at $\eta_{\rm lip}^{\rm res} = 0.5$. The stability at the contact distance, (a) $r = 3.0$ nm and (b) $r = 6.2$ nm, for the modified AO potential is much larger than that for the AO potential. The ratio is larger than three in the case of the bR monomers (FIG. 3.1(a)), and larger than four in the case of the bR trimer (FIG. 3.1(b)). That is, the effective attraction for the modified AO potential is much stronger than that for the AO potential.

Here, I mention the difference between the AO and the modified AO potentials. I prepared the pressure in calculating the quasistatic PV-work to change the excluded volume of bRs for the lipid fluid. In the case of the AO potential, the pressure of the ideal gas was used. On the other hand, 2D–SPT was adopted in the case of the modified AO potential. The latter pressure is higher than the former because of the packing effect of the lipid hard disks. Therefore, the stability of the contact bR dimer for the modified AO potential is much larger than that for the AO potential.

To obtain the phase diagrams, the thermodynamic perturbation theory was adopted. In the perturbation theory, the Helmholtz free energy for the effective one-component system with $\omega_{\rm AO}$ or ω_{Mod}, $F(N_{\rm bR}, V, T)$, was expressed as follows:

$$\frac{\beta F(N_{\rm bR}, V, T) v_{\rm bR}}{V} = \frac{\beta F_0(N_{\rm bR}, V, T) v_{\rm bR}}{V} + 4\beta\eta_{\rm bR}^2 \int_0^\infty g_0\left(\frac{r}{\sigma_{\rm bR}}\right) \omega\left(\frac{r}{\sigma_{\rm bR}}\right) \frac{r}{\sigma_{\rm bR}} d\left(\frac{r}{\sigma_{\rm bR}}\right), \tag{3.9}$$

where V is the area of the system, $v_{\rm bR}$ is the area of one bR, F_0 is the Helmholtz free energy for the pure bR system, $\eta_{\rm bR}$ is the packing fraction of the bRs, $\omega(\frac{r}{\sigma_{\rm bR}})$ is the

effective potential between bRs, and $g_0(\frac{r}{\sigma_{\rm bR}})$ is the radial distribution function for the pure bR system scaled by $\sigma_{\rm bR}$.

In the previous paragraph, the calculation of the perturbation part needed the radial distribution function. The radial distribution functions were obtained using the event chain Monte Carlo simulation [37]. The simulation box has 128^2 hard disks, and the sampling was carried out over 1.2×10^{11} steps after equilibration. The radial distribution functions were calculated within the ranging from $\eta_{\rm bR} = 0.001$ to $\eta_{\rm bR} = 0.905$ in the interval of $\eta_{\rm bR} = 0.001$. The AO or the modified AO potential were substituted in $\omega(\frac{r}{\sigma_{\rm bR}})$.

F_0 was obtained by the same method in the chapter 2. F_0 is:

$$\frac{\beta F_0 v_{\rm bR}}{V} = \beta \eta_{\rm bR} \mu^0_{\rm bR} - \beta p^0 v_{\rm bR}, \tag{3.10}$$

where $\mu^0_{\rm bR}$ and p^0 are the chemical potential and the pressure for the pure bR system. The chemical potential and the pressure for the pure bR fluid phase, $\mu^0_{\rm f}$ and $p^0_{\rm f}$, were obtained by 2D-Carnahan-Staring like equation of state (2D–CSE) [1, 46], as follows:

$$\beta \mu^0_{\rm f} = \ln\left[\frac{\Lambda^2}{v_{\rm bR}}\right] + \ln\left[\eta_{\rm bR}\right] - \frac{7}{8}\ln\left[1-\eta_{\rm bR}\right] + \frac{7}{8\left(1-\eta_{\rm bR}\right)} + \frac{9}{8\left(1-\eta_{\rm bR}\right)^2} - 2, \tag{3.11}$$

$$\beta p^0_{\rm f} v_{\rm bR} = \frac{\eta_{\rm bR} + \frac{(\eta_{\rm bR})^2}{8}}{\left(1-\eta_{\rm bR}\right)^2}, \tag{3.12}$$

where $\Lambda = {\rm h}(2\pi m_{\rm bR} {\rm k_B} T)^{-1/2}$ is the thermal de Broglie wavelength in the 2D space. h and $m_{\rm bR}$ are the Planck constant and the mass for a bR, respectively. The chemical potential and the pressure for the pure bR ordered phase, $\mu^0_{\rm ord}$ and $p^0_{\rm ord}$, were obtained by cell theory [46, 65] as follows:

$$\beta \mu^0_{\rm ord} = \ln\left[\frac{\Lambda^2}{v_{\rm bR}}\right] - 2\ln\left[\frac{\eta_{\rm cp}}{\eta_{\rm bR}} - 1\right] + \frac{2\eta_{\rm cp}}{\eta_{\rm cp} - \eta_{\rm bR}}, \tag{3.13}$$

$$\beta p^0_{\rm ord} v_{\rm bR} = \frac{2\eta_{\rm bR}}{1 - \frac{\eta_{\rm bR}}{\eta_{\rm cp}}}, \tag{3.14}$$

where $\eta_{\rm cp} = \pi/(2\sqrt{3}) \approx 0.907$ is the packing fraction at close packing. The first term on the right-hand side, $\ln\left[\frac{\Lambda^2}{v_{\rm bR}}\right]$, in eq. (3.11), and eq. (3.13) does not affect the phase diagram, because the term is common in the fluid and ordered phases. The common tangent method was adopted to obtain the phase diagrams using free energy curves. The common tangent was drawn on the calculated free energy curves for the fluid and ordered phase.

3.3 Phase diagrams obtained by using thermodynamic perturbation theory with AO or modified AO potential

The Helmholtz free energy curves were calculated using the thermodynamic perturbation theory with the effective potential. The phase diagrams were obtained using the common tangent construction on the free energy curves. The phase diagrams are shown in FIG. 3.2 for bR (a) monomers and (b) trimers calculated using the AO or the modified AO potentials as the effective potential.

The coexistence region for the modified AO potential expands at a lower lipid packing fraction than the AO potential. Here, I checked the diagram for the monomers with

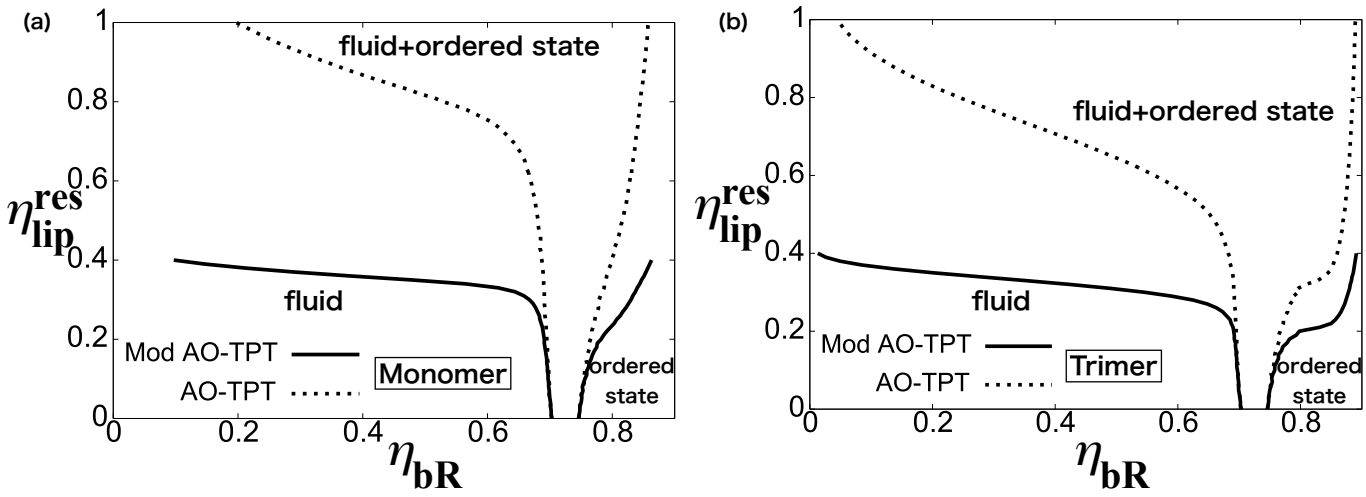

Figure 3.2: Phase diagrams for (a) bR monomer ($q = 0.16667$) and (b) trimer ($q = 0.08065$). The dotted curves show the phase diagram calculated by the thermodynamic perturbation theory(TPT) with the AO potential. The solid curves show the phase diagram calculated by the thermodynamic perturbation theory with the modified AO potential.

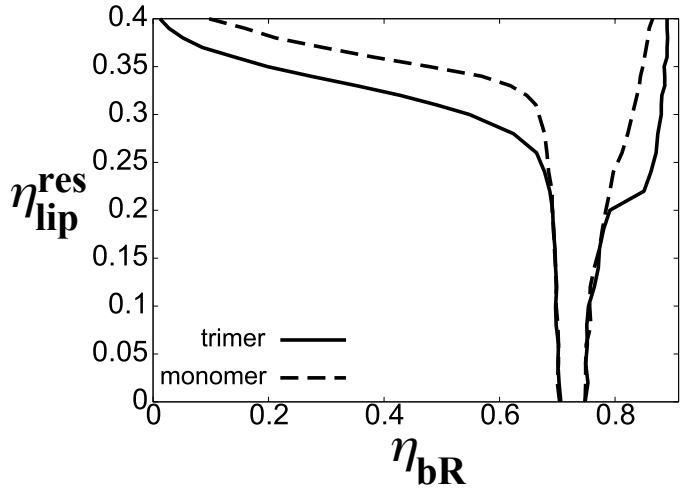

Figure 3.3: Phase diagrams for bR monomer and trimer calculated using the modified AO–TPT approach. The solid curves show the phase diagrams for the trimer. The dashed curves show the phase diagrams for the monomer.

the lipids (see FIG. 3.2 (a)). The broadening for the modified AO potential (solid curve) started at about $\eta_{\rm lip}^{\rm res} = 0.35$, although that for the AO potential (dashed curve) started at about $\eta_{\rm lip}^{\rm res} = 0.7$. I focused on the phase diagrams around $\eta_{\rm lip}^{\rm res} = 0.5$ because I estimated the lipid packing fraction of a cell membrane as 0.5 (see the chapter 2). The broadenings of the coexistence regions for the modified AO potential started lower than $\eta_{\rm lip}^{\rm res} = 0.5$. On the other hand, those for the AO potential started higher than $\eta_{\rm lip}^{\rm res} = 0.5$ (see FIG. 3.2 (a) and (b)). Therefore, effective potential dependence is critical.

The critical concentration, CC($\eta_{\rm lip}^{\rm res}$), was defined as the concentration for the smallest packing fraction for the fluid–ordered phase coexistence state at $\eta_{\rm lip}^{\rm res}$. Thus, the CC($\eta_{\rm lip}^{\rm res}$) gives the boundary curve between the fluid and fluid–ordered states [46]. Unfortunately, I could not obtain the phase diagrams for the modified AO potential systems in the region $\eta_{\rm lip}^{\rm res} > 0.4$ (see solid curves in FIG.3.2), because the phase diagram cannot

be calculated by modified AO–TPT approach when the CC is very low. This is because that the common tangent cannot be drawn on the free energy. However, the CC is almost 0 even when $\eta_{\mathrm{lip}}^{\mathrm{res}} = 0.4$. Therefore, it is expected that the CC is very low when $\eta_{\mathrm{lip}}^{\mathrm{res}} = 0.5$. This suggests that the depletion effect can be dominant in the driving force for the bR ordering.

The phase diagrams calculated using modified AO potential for monomer and trimer are compared in FIG. 3.3. FIG. 3.3 shows that the the coexistence region for the trmer is wider than that for the monomer. That is, the CC for trimer is lower than that for the monomer. This result indicates that the depletion effect for the trimer is stronger than that for the monomer.

3.4 Second virial coefficients for AO and modified AO potential

The second virial coefficient (B_2) is useful for discussing whether the particles are attractive or repulsive. I explain the B_2. The pressure is expanded by number density, ρ, as follows:

$$\beta p = \rho + B_2\rho^2 + O(\rho^3), \tag{3.15}$$

where the coefficient of ρ^2 is the B_2. The B_2 is an index for the attraction or the repulsion of the interaction. The equation of state for an ideal gas is

$$\beta p = \rho. \tag{3.16}$$

Thus, the B_2 is zero.

When the B_2 is positive, the pressure is higher than that for the ideal gas. That is, the effective interaction between particles is more repulsive than the ideal gas. On the other hand, when the B_2 is negative, the pressure is lower than that for ideal gas. That is, the effective interaction is more attractive than the ideal gas. Here, the B_2 for the 2D case is calculated as follows:

$$B_2 = -\pi \int r(\exp[-\beta u(r)] - 1)\mathrm{d}r, \tag{3.17}$$

where $u(r)$ is the pairwise potential and r is the distance between the centers of the particles. In this study, the effective interaction $w(r)$ was substituted into the potential $u(r)$. Therefore, the B_2 is the effective second virial coefficient. This B_2 was scaled by the B_2 for hard–disks, ${B_2}^{\mathrm{HD}}$. $B_2/{B_2}^{\mathrm{HD}}$ is the reduced (effective) second virial coefficient.

Two effective potentials between two large hard–disks (proteins) were examined. One is the conventional AO potential [7]. The other is a modified AO potential. In the AO theory, the depletants (lipid molecules, small disks) do not interact with each other. In other words, the depletants are ideal gas molecules. By contrast, for the modified AO potential, the attraction between two large disks at the contact distance is stronger than that for the conventional AO potential, because the pressure exerted by the depletants to the large disks is calculated by using the 2D–SPT. This is because the repulsion between depletants is not ignored in the 2D–SPT and the pressure becomes larger than that of an ideal gas.

FIG. 3.4 indicates the q-dependence of the coefficient B_2/B_2^{HD} (a) for modified AO and (b) for AO. The negative values appear at around $\eta_{\mathrm{lip}}^{\mathrm{res}} = 0.35$ in the plot for modified AO (FIG. 3.4 (a)). In the plot for $\eta_{\mathrm{lip}}^{\mathrm{res}} = 0.35$, the coefficient B_2/B_2^{HD} is almost zero. In addition, the negative value appears when q is below 0.11. This suggests that the particles are attractive and the wide coexistence region can appear. This result is consistent with the phase diagrams with the modified AO potential. However, the absolute value is still small when $\eta_{\mathrm{lip}}^{\mathrm{res}} = 0.35$.

As the packing fraction $\eta_{\mathrm{lip}}^{\mathrm{res}}$ becomes larger, the value B_2/B_2^{HD} decreases. The B_2/B_2^{HD} for modified AO is smaller than 0 for any q when the $\eta_{\mathrm{lip}}^{\mathrm{res}}$ is larger than 0.36.

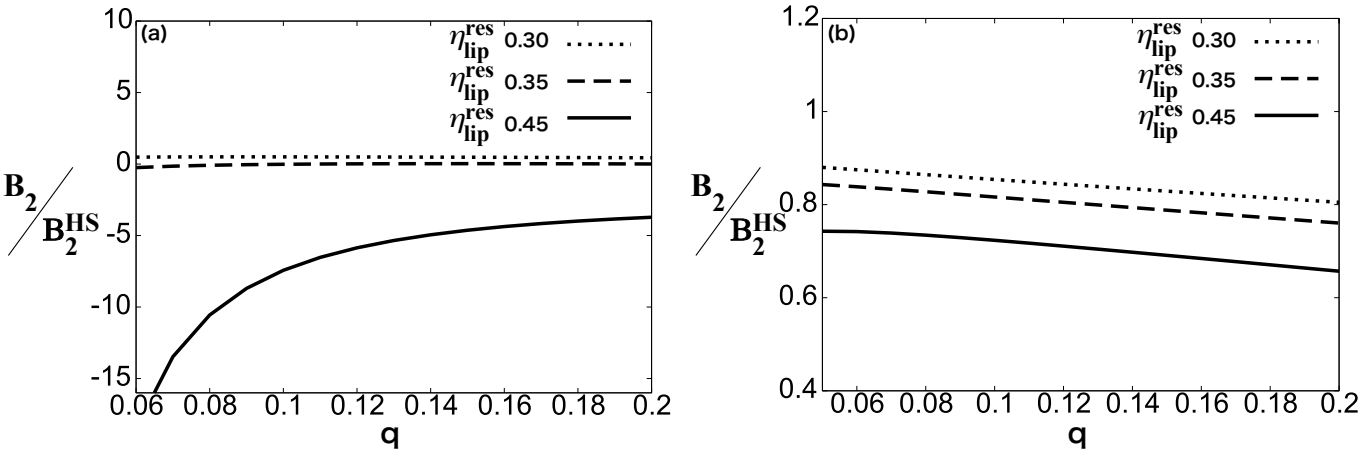

Figure 3.4: The reduced second virial coefficient of large disks (bRs) for modified AO (a) and for AO (b) when the small disks (lipid molecules) packing fraction is 0.30 (dotted curve), 0.35 (dashed curve), and 0.45(solid curve).

When the $\eta_{\rm lip}^{\rm res}$ is 0.45, the absolute value of $B_2/B_2^{\rm HD}$ for modified AO becomes very large because of the effective attraction. It is about -7.4 at $q = 0.1$, and the appearance of a condensation phase is expected. In addition, FIG. 3.4 (a) shows that the $B_2/B_2^{\rm HD}$ for $\eta_{\rm lip}^{\rm res} = 0.45$ increases monotonically as the q increases. As I mentioned in the section 3.3, the depletion attraction between bR trimers is stronger than that between monomers. Thus, these results for the $B_2/B_2^{\rm HD}$ are consistent with the phase diagrams shown in the section 3.3.

By contrast, the plots for AO do not have negative values even when $\eta_{\rm lip}^{\rm res} = 0.45$ (FIG. 3.4 (b)). This means that the particles in the system are repulsive. If $\eta_{\rm lip}^{\rm res}$ becomes larger, the coefficient $B_2/B_2^{\rm HD}$ becomes negative. However, the value $\eta_{\rm lip}^{\rm res}$ becomes unphysical. The Phase diagrams with AO potential does not show the expansion of the coexistence region at $\eta_{\rm lip}^{rmres} = 0.5$, and this result is consistent with the $B_2/B_2^{\rm HD}$. In addition, a comparison between the $B_2/B_2^{\rm HD}$ values for modified AO and AO indicates that the repulsive forces between lipid molecules are important for the association of bRs.

3.5 Comparison of phase diagrams between thermodynamic approach and free volume approach

Here, I compared the phase diagrams obtained using the modified AO–TPT approach with that obtained using the 2D–FVT approach. In the chapter 2, the chemical potentials for the fluid and ordered phases were described using the two-dimensional Carnahan-Starling-like equation of state (2D–CSE) and the cell theory in the case of the pure bR system ($\eta_{\rm lip}^{\rm res} = 0$). Thus, the reference systems in both approaches are common. Additionally, I adopted the pressure of the two-dimensional scaled particle theory (2D–SPT) as the reservoir pressure. This means that the repulsive cores of the lipids in the reservoir are common between the two approach. However, the framework of 2D–FVT did not explicitly contain the effective interaction between two bRs [46]. On the other hand, the modified AO potential was adopted as the effective interaction and the phase diagrams were calculated using the thermodynamic perturbation theory with the effective interaction (modified AO–TPT) in the present study. The results are compared in FIG.3.5.

Because the theories of the reference systems, namely the pure bR system ($\eta_{\rm lip}^{\rm res} = 0$), are common, the coexistence region appears in the same region (see FIG. 3.5). Even when $\eta_{\rm lip}^{\rm res}$ increases, the phase diagrams of the 2D–FVT approach are in good agreement

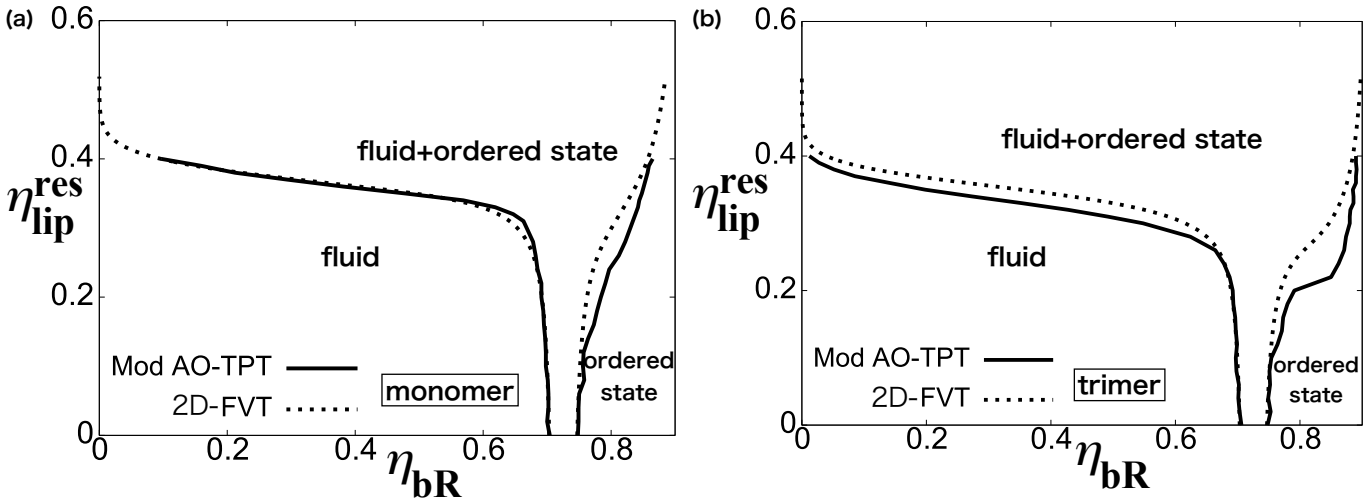

Figure 3.5: Phase diagrams for (a) bR monomer ($q = 0.16667$) and (b) trimer ($q = 0.08065$). The solid curves show the phase diagrams calculated by the modified AO–TPT approach. The dotted curves show the phase diagrams calculated by the 2D– FVT approach [46].

with the results given by the modified AO–TPT study. In particular, the boundaries between the fluid and the fluid–ordered coexistence phases in the modified AO–TPT approach agree very well with the results of 2D–FVT approach. In the chapter 2, I showed that the 2D–FVT approach explains the experimental results semi-quantitatively [46]. Therefore, it is expected that the modified AO–TPT approach is also valid.

On the other hand, there is a difference between phase diagrams for the bR trimer calculated by modified AO–TPT and 2D–FVT approaches. The coexistence region calculated by the modified AO–TPT approach is slightly wider than that calculated by the 2D–FVT approach. This difference increases as the size ratio q approaches 0 (data is not shown). I cannot deny the problem in the modified AO–TPT approach. However, the results of the 2D–FVT approach are more suspicious because the q-dependence on the phase diagram disappears at the small q as shown in the chapter 2. The CC for the trimer seems to be higher than the real CC because of the existence of lower limit of CC at small q in the 2D–FVT approach.

However, the CC for the bR trimer ordering is lower than for the monomer ordering in both theories. For example, when $\eta_{\rm lip}^{\rm res} = 0.4$, the CCs for bR monomer ordering and trimer ordering calculated by the 2D–FVT approach are 0.100 and 0.042, respectively [46]. On the other hand, the CCs for the bR monomer ordering and the trimer ordering calculated by the modified AO–TPT approach are 0.097 and 0.013, respectively. The CC for the bR trimer ordering is lower than that for the monomer ordering in each theory. These results correspond to experimental results [45] qualitatively. As with the 2D–FVT approach [46], the modified AO–TPT approach also explains the experimental results for bR crystallization [45] qualitatively.

3.6 Comparison of CCRs between thermodynamic perturbation theory approach and free volume theory approach

FIG. 3.6 (a) shows the critical concentration ratios (CCRs) between bR monomer and trimer (CC monomer/ CC trimer) obtained from the phase diagrams calculated using the modified AO–TPT approach (symbol). The curves are drawn by sixth-order polynomial approximation when $\sigma_{\rm lip} = 0.5$ and 0.6 nm. On the other hand, the polynomial

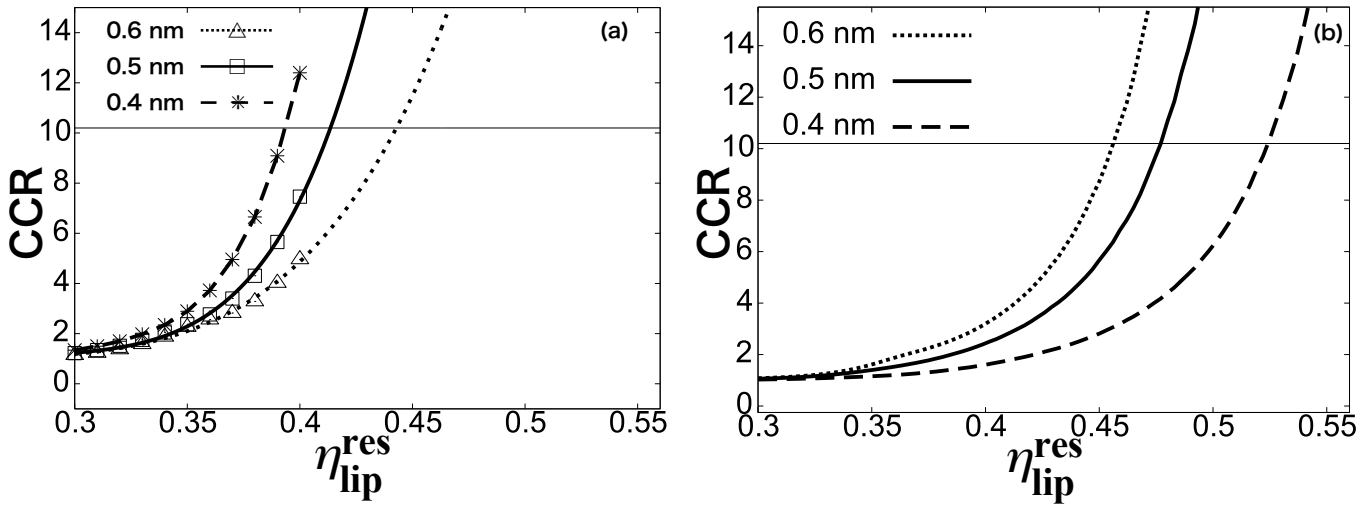

Figure 3.6: (a) The CCRs were calculated by the modified AO–TPT approach. The triangles, squares, and asterisks show the CCR for $\sigma_{\rm lip} = 0.4$, 0.5, and 0.6, respectively. A dashed line shows the CCR for $\sigma_{\rm lip} = 0.4$. A solid and dotted lines show the sixth-order polynomial approximation curves of CCR for $\sigma_{\rm lip} = 0.5$ and 0.6, respectively. The experimental value of the CCR, 10.2, is shown as a thin solid line parallel to the x–axis. (b) The CCRs were calculated by the 2D–FVT approach. The dotted line, a solid line, and a dashed line show the CCR for $\sigma_{\rm lip} = 0.4$, 0.5, and 0.6, respectively [46].

approximation for $\sigma_{\rm lip} = 0.4$ nm is not drawn because the data are across the line for the CCR=10.2. FIG.3.6 (b) has the CCR plots calculated by the 2D–FVT approach in the chapter 2 for comparison. The diameter of the lipid molecule is 0.5 nm as a standard. However, this model has arbitrariness. The three lipid diameters $\sigma_{\rm lip} = 0.4$, 0.5, and 0.6 nm, were examined to remove the arbitrariness. The experimental value of the CCR, 10.2, is shown as a solid line parallel to the x–axis. When the CC is too low, the phase diagram cannot be obtained using the TPT approach with the modified AO interaction because the common tangent cannot be drawn on the free energy curves. Therefore, the CCR cannot be calculated up to 10.2. Thus, the extrapolated plots were drawn when $\sigma_{\rm lip} = 0.5$ and 0.6 nm. The CCR increases in each theory as $\eta_{\rm lip}^{\rm res}$ increases.

The CCRs obtained by the modified AO–TPT approach and the 2D–FVT approach were compared. In the modified AO–TPT approach, the maximum $\eta_{\rm lip}^{\rm res}$ where CC can be calculated for all lipid diameters was 0.40. At $\eta_{\rm lip}^{\rm res}$ =0.40, the CCRs obtained by the two approaches were compared. When the $\sigma_{\rm lip}$ is 0.4 nm, the CCR obtained by the modified AO–TPT approach was 12.4. On the other hand, the CCR obtained by the 2D–FVT approach was 1.60. When the $\sigma_{\rm lip}$ is 0.5 nm, the CCR obtained by the modified AO–TPT approach was 7.46. On the other hand, the CCR obtained by the 2D–FVT approach was 2.43. When the $\sigma_{\rm lip}$ is 0.6 nm, the CCR obtained by the modified AO–TPT approach was 4.96. On the other hand, the CCR obtained by the 2D–FVT approach was 3.18. The CCR obtained by the modified AO–TPT approach was larger than that obtained by the 2D–FVT approach for all $\sigma_{\rm lip}$. This is because the CC for trimer calculated by the modified AO–TPT approach is smaller than that calculated by the 2D–FVT approach, while the CC for monomer is almost the same between the two theories. The difference of the trimer CC is more significant as the $\sigma_{\rm lip}$ is smaller, i.e. q is smaller. The reason seems to be that the CC at smaller q is more affected by the lower limit of CC in the 2D–FVT approach.

The extrapolated CCR plots obtained by the modified AO–TPT approach agree with experimental CCR value 10.2 at $\eta_{\rm lip}^{\rm res} = 0.393$, 0.414, 0.443 for $\sigma_{\rm lip} = 0.4$, 0.5, 0.6

nm, respectively. $\eta_{\mathrm{lip}}^{\mathrm{res}}$s correspond to the lipid number densities 3.13, 2.11, and 1.57 $\times 10^6 \mu m^{-2}$, respectively. On the other hand, the lipid number density in the single layer of a cell membrane was about 2.5 $\times 10^6 \mu m^{-2}$ [30]. Therefore, the CCRs obtained using modified AO–TPT approach also show the good agreement with experimental results semi-quantitatively.

A qualitative difference of CCRs between the 2D–FVT and modified AO–TPT approaches are found. Comparing FIG. 3.6 (a) and (b), the CCRs order of the dependence on the lipid diameter for the modified AO–TPT approach is the inverse of that for the 2D–FVT approach. The CCRs obtained by the 2D–FVT approach increase as the lipid diameter increases. In contrast, the CCRs obtained by the modified AO–TPT approach decrease as the lipid diameter increases. This discrepancy seems to be caused by a problem in the 2D–FVT approach: namely, the calculation of CC for the trimer. The order for the 2D–FVT approach seems to be incorrect because of the disappearance of the q-dependence at small q. The CC for the trimer decreases as q decreases. However, in the 2D–FVT approach, the decrease is braked due to the lower limit of CC at small q. On the other hand, the CC for the monomer is not braked because the q is not small. Thus, the CC decline for the trimer with the q decline is smaller than that for the monomer. On the other hand, in the modified AO–TPT approach, the CC decline for the trimer is larger than that for the monomer because there is no lower limit of CC. Therefore, the CCR order obtained using the 2D–FVT approach is inverse of that obtained using modified AO–TPT approach, and incorrect.

3.7 Discussion

The calculated results indicate that the experimental results are explained by using the modified AO potential. However, the modified AO potential is based on very simple idea, and has incompleteness. The modified AO potential does not have a local maximum. On the other hand, a real effective potential has local maximum at around $r = (\sigma_{\mathrm{bR}} + \sigma_{\mathrm{lip}})/2$. This is because that, the lipid molecules around the bR prevent the contact between bRs. That is, the modified AO potential does not contain the liquid structure of lipid molecules. The ignorance of the liquid structure of solvents may change the phase diagram. Therefore, the phase diagrams should be confirmed by simulation.

3.8 Summary

The phase diagrams of binary hard-disk systems were calculated to discuss the driving force of bR crystallization. To study the effects of the core repulsive force between lipid molecules as depletants, I calculated the phase diagram and CCR using the thermodynamic perturbation theory with two effective interactions between bRs [70–72]. The approach was entirely different from the study in section 2 based on the 2D–FVT approach [46]. The 2D–FVT approach has problem when q is very small. However, the CCR obtained using the modified AO–TPT approach also showed good agreement with the experimental results semi-quantitatively as with the 2D–FVT approach. Therefore, the present results also support that the depletion effect arising from the lipid molecules plays an essential role in the driving force of crystallization. In the future, I think that verification by simulation should be necessary.

Chapter 4

Conclusion

I assumed the driving force for the bR ordering as the depletion force of lipid molecules and examined the validity of that assumption. Experiments conducted by M. P. Krebs et. al. showed that bR monomers start to crystalize in 10.2 times higher bR packing fraction than trimers. I explained this result by the depletion force theoretically. The bR phase diagrams were calculated and the critical concentration ratio (CCR) was obtained from the phase diagrams. The calculated CCRs were compared with experimental CCR. The CCRs were obtained by two approaches, namely the two-dimensional free volume theory (2D–FVT) and the thermodynamic perturbation theory with effective potential. The results are summarized as follows, respectively.

First, I calculated the phase diagrams for the bR monomers and trimers by using 2D —FVT approach. When the lipid molecules in the reservoir are modeled as ideal gas, the fluid–ordered phase coexistence region does not expand and the critical concentration (CC) for the ordering stays high at the lipid packing fraction of the biomembrane, namely 0.5. On the other hand, when the repulsive interaction between lipid molecules is considered, the coexistence region expands, and the CC is very small at the lipid packing fraction $= 0.5$. Therefore, it is indicated that the depletion force is strong enough to drive the bR ordering when the repulsive interaction between lipid molecules is considered. In addition, the CC for the monomer is higher than that for the trimer and the calculated CCR agrees with the experimental CCR. These results indicate that the depletion force of lipid molecules is the driving force for the bR ordering.

I adopted AO potential or modified AO potential as the effective potential, and phase diagrams were obtained by using thermodynamic perturbation theory (TPT). The model is the same as that adopted in the 2D—FVT approach. When I adopted the AO potential, which did not contain the repulsion between lipid molecules, the coexistence region did not expand, and the CC did not decrease. On the other hand, When I adopted the modified AO potential, which contain the repulsion between lipid molecules, the coexistence region expanded, and the CC was very small. As with the 2D—FVT approach, it is indicated that the depletion force is strong enough to drive the bR ordering when the repulsive interaction between lipid molecules is considered. In addition, the phase diagrams shows that the CC for monomer is higher than that for the trimer, and the CCR shows good agreement with experimental CCR. The results calculated by modified AO —TPT approach also indicate that the depletion force of lipid molecules is the driving force for the ordering.

I showed that the depletion force seems to be dominant for the bR ordering. However, the model and the theory are very simple, and I ignore some aspects of bR crystallization. First, I model the biomembrane as a lipid monolayer, although the biomembrane is a lipid bilayer. Thus, the lipid number density is half of the real biomembrane, and the depletion force seems to be half of the actual effective force. Second, I modeled the bR as the disk which has a smooth surface, although the bR has a bumpy surface.

Lipid molecules are in gap between the bumpy surfaces of two bRs [73]. Therefore, the actual bR crystal has more lipid molecules than calculation in this thesis. According to experimental research [74], the lipid molecules in the bR crystal may be important for the crystallization. To examine the effect of these aspects on the bR crystallization, further research must be done.

Acknowledgements

This work was supported by Grant-in-Aid for Japan Society for the Promotion of Science (JSPS) Fellows Number JP22J13118. The computation was performed using Re- search Center for Computational Science, Okazaki, Japan (Project: 22-IMS- C101 and 22-IMS-C113) and the Research Institute for Information Technology, Kyushu University.

I am grateful to Associate Professor Ryo Akiyama for guiding my study. I would like to thank to Specially-Appointed Lecturer Ayumi Suematsu (Kyushu Sangyo University) and Associate Professor Yuki Uematsu (Kyushu Institute of Technology) for their comments and assistance for numerical calculations. I also thank the members of the Chemical Physics and Biophysics group in Kyushu University. In addition, I am grateful to my family for their kind support of my life.

Appendix A

Derivation of Semi-grand potential by free volume theory

Here, I derive the semi-grand potential $\Omega\left(N_{\mathrm{bR}}, V, T, \mu_{\mathrm{lip}}\right)$ in eq. (). The 2D binary hard disk system with the reservoir of lipid molecules is considered. Ω is obtained by Legendre transformation of Helmholtz free energy $F\left(N_{\mathrm{bR}}, V, T, N_{\mathrm{lip}}\right)$ as follows

$$\Omega\left(N_{\mathrm{bR}}, V, T, \mu_{\mathrm{lip}}\right) = F\left(N_{\mathrm{bR}}, V, T, N_{\mathrm{lip}}\right) - \mu_{\mathrm{lip}} N_{\mathrm{lip}} \tag{A.1}$$

where N_{bR} is the number of bRs, V is the area of binary hard disk system, T is the temperature, μ_{lip} is the chemical potential for the lipid molecules, and N_{lip} is the number of lipid molecules. On the other hand, by differentiating Ω by μ_{lip}, the N_{lip} is obtained as follows:

$$\left(\frac{\partial \Omega}{\partial \mu_{\mathrm{lip}}}\right)_{N_{\mathrm{bR}}, T, V} = -N_{\mathrm{lip}}. \tag{A.2}$$

Thus, Ω is also written as

$$\Omega\left(N_{\mathrm{bR}}, V, T, \mu_{\mathrm{lip}}\right) = \Omega_0\left(N_{\mathrm{bR}}, V, T, \mu_{\mathrm{lip}}^0\right) - \int_{\mu_{\mathrm{lip}}^0}^{\mu_{\mathrm{lip}}} N_{\mathrm{lip}} d\mu'_{lip}, \tag{A.3}$$

where Ω_0 and μ_{lip}^0 are the semi-grand potential and the chemical potential for the lipid molecules in reference system. The bR pure system, i.e. $N_{\mathrm{lip}} = 0$, is adopted as the reference system. Here, $\Omega_0\left(N_{\mathrm{bR}}, V, T, \mu_{\mathrm{lip}}^0\right) = F\left(N_{\mathrm{bR}}, V, T\right)$. I define the Helmholtz free energy for the bR pure system as $F_0\left(N_{\mathrm{bR}}, V, T\right)$ Thus, the Ω is

$$\Omega\left(N_{\mathrm{bR}}, V, T, \mu_{\mathrm{lip}}\right) = F_0\left(N_{\mathrm{bR}}, V, T\right) - \int_{-\infty}^{\mu_{\mathrm{lip}}} N_{\mathrm{lip}} d\mu'_{lip}. \tag{A.4}$$

To calculate the integral, Widom insertion Theorem is adopted. The chemical potential for hard disk is calculated by the theorem as follows:

$$\mu_{\mathrm{lip}} = C + \mathrm{k_B} T \ln \frac{N_{\mathrm{lip}}}{\langle V_{\mathrm{free}} \rangle}, \tag{A.5}$$

where C is a constant, $\mathrm{k_B}$ is the Boltzmann constant, and V_{free} is the free volume for one lipid molecule in the binary hard disk system. Here, the chemical potential for lipid molecules in the reservoir,$\mu_{\mathrm{lip}}^{\mathrm{res}}$, is also written as follows:

$$\mu_{\mathrm{lip}}^{\mathrm{res}} = C + \mathrm{k_B} T \ln \frac{N_{\mathrm{lip}}^{\mathrm{res}}}{\left\langle V_{\mathrm{free}}^{\mathrm{res}} \right\rangle}, \tag{A.6}$$

where $N_{\mathrm{lip}}^{\mathrm{res}}$ is the lipid number in the reservoir and $V_{\mathrm{free}}^{\mathrm{res}}$ is the free volume in the reservoir. From the eqs. (A.5) and (A.6), an equation is obtained as follows:

$$N_{\mathrm{lip}} = \langle V_{\mathrm{free}} \rangle \rho_{\mathrm{lip}}^{\mathrm{res}}, \tag{A.7}$$

where $\rho_{\text{lip}}^{\text{res}}$ is the lipid number density in the reservoir. Substituting the eq. (A.7), the eq.(A.4) is

$$\Omega\left(N_{\text{bR}}, V, T, \mu_{\text{lip}}\right) = F_0\left(N_{\text{bR}}, V, T\right) - \int_{-\infty}^{\mu_{\text{lip}}} \langle V_{\text{free}} \rangle \rho_{\text{lip}}^{\text{res}} d\mu'_{lip}. \tag{A.8}$$

To calculate the integral, the Gibbs-Duhem relation,

$$\rho_{\text{lip}}^{\text{res}} d\mu_{\text{lip}} = dp^{\text{res}} \tag{A.9}$$

is adopted. The eq. (A.8) is

$$\Omega\left(N_{\text{bR}}, V, T, \mu_{\text{lip}}\right) = F_0\left(N_{\text{bR}}, V, T\right) - \langle V_{\text{free}} \rangle p^{\text{res}}. \tag{A.10}$$

Appendix B

Derivation of free volume fraction, pressure and chemical potential for bR pure system

B.1 Derivation of free volume fraction by scaled particle theory

Free volume fraction α is calculated by using scaled particle theory (SPT). The 2D binary hard disk system with the reservoir of lipid molecules is considered. Adopting the Widom insertion theorem, the chemical potential for the lipid molecule,μ_{lip}, is written as follows

$$\mu_{\mathrm{lip}} = C + \mathrm{k_B} T \ln \frac{N_{\mathrm{lip}}}{\langle V_{\mathrm{free}} \rangle_0}, \tag{B.1}$$

where C is constant, $\mathrm{k_B}$ is the Boltzmann constant, T is the temperature, N_{lip} is the number of lipid, and $\langle V_{\mathrm{free}} \rangle_0$ is the free volume for one lipid molecule in the bR pure system. Here, I adopted an approximation that replace $\langle V_{\mathrm{free}} \rangle$ to $\langle V_{\mathrm{free}} \rangle_0$. The μ_{lip} is also written by using work, W, to insert one lipid molecule to the bR pure system as follows:

$$\mu_{\mathrm{lip}} = C + \mathrm{k_B} T \ln \frac{N_{\mathrm{lip}}}{V} + \mathrm{W}, \tag{B.2}$$

where V is the area of binary hard disk system. Comparing the eqs. (B.1) and (B.2), an equation is obtained as follows:

$$\frac{\langle V_{\mathrm{free}} \rangle_0}{V} = \exp\left[-\beta \mathrm{W}\right]. \tag{B.3}$$

W depends on the diameters of lipid molecule and bR. Here, the diameter of the lipid is σ and that of the bR is $2R$. To adopt the SPT, σ is scaled by an parameter λ. When λ is small, the diameter of lipid is small. On the other hand, when λ is large, the diameter of lipid is large. In the case of $\lambda << 1$, the overlap area of excluded volume can be ignored, and the free volume fraction is

$$\frac{\langle V_{\mathrm{free}} \rangle_0}{V} = \frac{V - \frac{\pi}{4}\left(2R + \lambda\sigma\right)^2 N_{\mathrm{bR}}}{V}. \tag{B.4}$$

Therefore, W is

$$W = -\mathrm{k_B} T \ln\left[1 - \rho_{\mathrm{bR}} \frac{\pi}{4}\left(2\mathrm{R} + \lambda\sigma\right)\right], \tag{B.5}$$

where ρ_{bR} is the number density of bR. In the case of $\lambda >> 1$, W is p-V work to create a vacuum space for one lipid molecule. Thus, W is

$$W = p\frac{\pi}{4}\left(\lambda\sigma\right)^2, \tag{B.6}$$

wherw p is the pressure. The SPT assume that $W(\lambda)$ is the sum of W for $\lambda << 1$ and $\lambda >> 1$ as follows:

$$W(\lambda) = W(0) + \left(\frac{\partial W}{\partial \lambda}\right)_{\lambda=0} \lambda + p\frac{\pi}{4}\left(\lambda\sigma\right)^2. \tag{B.7}$$

The first and second term in the right side are the Maclaurin expansion of W for $\lambda << 1$. The third term is the W for $\lambda >> 1$. Substituting the p calculated by SPT, $p = \frac{\rho_{bR} k_B T}{(1-\eta_{bR})^2}$, and $\lambda = 1$, W is

$$\beta W = -\ln[1-\eta_{bR}] + \frac{2\eta_{bR} q}{1-\eta_{bR}} + \frac{\eta_{bR} q^2}{(1-\eta_{bR})^2}, \tag{B.8}$$

where q is the diameter ratio $\sigma/2R$ and η_{bR} is the packing fraction of bR. Thus, the free volume fraction is as follows

$$\frac{\langle V_{free}\rangle_0}{V} = (1-\eta_{bR}) \exp\left[-\frac{2\eta_{bR} q}{1-\eta_{bR}} - \frac{\eta_{bR} q^2}{(1-\eta_{bR})^2}\right]. \tag{B.9}$$

B.2 Derivation of pressure and chemical potential for bR pure system in fluid phase by scaled particle theory

Pressure for the bR pure system in the fluid phase is obtained by using scaled particle theory. W to insert one bR to bR pure system is obtained by substituting $q = 1$ to eq. (B.7) as follows:

$$\beta W = -\ln[1-\eta_{bR}] + \frac{2\eta_{bR}}{1-\eta_{bR}} + \beta v_0 p_f^0, \tag{B.10}$$

where v_0 is the area of one bR and p_f^0 is the pressure for bR pure system in the fluid phase. Chemical potential for bR pure system in the fluid phase is as follows:

$$\mu_f^0 = k_B T \ln \Lambda^2 + k_B T \ln \frac{N_{bR}}{V} + W, \tag{B.11}$$

where Λ is the thermal de Broglie wavelength in the 2D space, N_{bR} is the number of bR. Here, the Gibbs-Duhem relation,

$$\rho_{bR}\left(\frac{\partial \mu_f^0}{\partial \eta_{bR}}\right) = \left(\frac{\partial p_f^0}{\partial \eta_{bR}}\right), \tag{B.12}$$

is adopted to eq.(B.11). The eq. (B.11) is

$$\left(\frac{\partial \beta \mu_f^0}{\partial \eta_{bR}}\right) = \frac{\partial}{\partial \eta_{bR}}\left(\ln \frac{N_{bR}}{V}\right) - \frac{\partial}{\partial \eta_{bR}}\left(-\ln[1-\eta_{bR}] + \frac{2\eta_{bR}}{1-\eta_{bR}}\right) + v_0\left(\frac{\partial \beta p^0}{\partial \eta_{bR}}\right) = \frac{1}{\rho_{bR}}\left(\frac{\partial \beta p_f^0}{\partial \eta_{bR}}\right). \tag{B.13}$$

Thus, $\left(\frac{\partial p_f^0 v_0}{\partial \eta_{bR}}\right)$ is as follows:

$$(1-\eta_{bR})\left(\frac{\partial \beta p_f^0 v_0}{\partial \eta_{bR}}\right) = \frac{1}{1-\eta_{bR}} + \frac{2\eta_{bR}}{(1-\eta_{bR})^2}. \tag{B.14}$$

Therefore, p_f^0 is

$$\beta p_f^0 v_0 = \frac{\eta_{bR}}{(1-\eta_{bR})^2}. \tag{B.15}$$

Substituting the eq. (B.15) to the eq. (B.10), W is

$$\beta W = -\ln[1-\eta_{bR}] + \frac{2\eta_{bR}}{1-\eta_{bR}} + \frac{\eta_{bR}}{(1-\eta_{bR})^2}. \tag{B.16}$$

The eq. (B.16) is substituted to the eq. (B.11), the chemical potential is

$$\beta \mu_f^0 = \ln\left[\frac{\Lambda^2}{v_{bR}}\right] + k_B T \ln\left[\frac{\eta_{bR}}{1-\eta_{bR}}\right] + \frac{2-\eta_{bR}}{(1-\eta_{bR})^2} - 2. \tag{B.17}$$

B.3 Derivation of pressure and chemical potential for bR pure system in ordered phase

A partition function Q for bR ordered phase is calcluted by cell theory as follows:

$$Q = \frac{\langle v* \rangle^{N_{\mathrm{bR}}}}{\Lambda^{2N_{\mathrm{bR}}}} \tag{B.18}$$

Here, $v*$ is area where one bR center can move in the hexagonal lattice shown as red zone in FIG. ??. The area of $v*$ is

$$\langle v* \rangle = \pi(r-2R)^2, \tag{B.19}$$

where r is distance between bR centers and R is the radius of bR. The Helmholtz free energy F is

$$F = -\mathrm{k_B}T\ln Q = -N_{\mathrm{bR}}\mathrm{k_B}T\ln\left[\pi(\mathrm{r}-2\mathrm{R})^2\right] + \mathrm{N_{bR}k_B}T\ln\Lambda^2. \tag{B.20}$$

The eq.(B.20) is rewritten by packing fraction η_{bR} and close packing η_{cp}. When the bRs construct hexagonal lattice, there are three bRs in the hexagon (FIG. ??). The area of the hexagon is $\frac{3\sqrt{3}r^2}{2}$. The area of bRs in the hexagon is $3v_{\mathrm{bR}}$. Thus,

$$\eta_{\mathrm{bR}} = \frac{2v_{\mathrm{bR}}}{\sqrt{3}r^2}. \tag{B.21}$$

At the close packing, $r = 2R$. Therefore,

$$\eta_{\mathrm{cp}} = \frac{\pi}{2\sqrt{3}} \approx 0.907. \tag{B.22}$$

Thus,

$$\frac{r}{2R} = \sqrt{\frac{\eta_{\mathrm{cp}}}{\eta_{\mathrm{bR}}}}. \tag{B.23}$$

Here, I calculate the eq.(B.20) as follows:

$$F = -N_{\mathrm{bR}}\mathrm{k_B}T\ln\left[\pi(2\mathrm{R})^2\left(\frac{\mathrm{r}}{2\mathrm{R}}-1\right)^2\right] + N_{\mathrm{bR}}\mathrm{k_B}T\ln\Lambda^2. \tag{B.24}$$

Substituting the eq.(B.23) to eq. (B.24),

$$F = -N_{\mathrm{bR}}\mathrm{k_B}T\ln\left[\left(\sqrt{\frac{\eta_{\mathrm{cp}}}{\eta_{\mathrm{bR}}}}-1\right)^2\right] + N_{\mathrm{bR}}\mathrm{k_B}T\ln\frac{\Lambda^2}{4\mathrm{v_{bR}}}. \tag{B.25}$$

Here, adopting the approximation,

$$\sqrt{\frac{\eta_{\mathrm{cp}}}{\eta_{\mathrm{bR}}}}-1 \approx \frac{1}{2}\left(\frac{\eta_{\mathrm{cp}}}{\eta_{\mathrm{bR}}}-1\right), \tag{B.26}$$

the eq. (B.25) is

$$F = -2N_{\mathrm{bR}}\mathrm{k_B}T\ln\left[\frac{\eta_{\mathrm{cp}}}{\eta_{\mathrm{bR}}}-1\right] + N_{\mathrm{bR}}\mathrm{k_B}T\ln\frac{\Lambda^2}{\mathrm{v_{bR}}}. \tag{B.27}$$

Thus, pressure and chemical potential for bR pure system in ordered phase are obtained by differentiating F as follows:

$$\beta p^0_{\mathrm{ord}} v_{\mathrm{bR}} = \frac{2\eta_{\mathrm{bR}}}{1-\eta_{\mathrm{bR}}/\eta_{\mathrm{cp}}}, \tag{B.28}$$

$$\beta\mu^0_{\mathrm{ord}} = \ln\left[\frac{\Lambda^2}{v_{\mathrm{bR}}}\right] - 2\ln\left[\frac{\eta_{\mathrm{cp}}}{\eta_{\mathrm{bR}}}-1\right] + \frac{2\eta_{\mathrm{cp}}}{\eta_{\mathrm{cp}}-\eta_{\mathrm{bR}}}. \tag{B.29}$$

References

[1] Henderson, R. and Unwin, P. N. T., Nature, (1975), **257**, 28.

[2] Henderson, R.; Baldwin, J. M.; Ceska, T. A.; Zemlin, F.; Beckmann, E. and Downing, K. H., J. Mol. Biol., (1990), **213**, 899.

[3] Mukai, Y.; Kamo, N. and Mitaku, S., Protein Eng., (1999), **12**, 755.

[4] Sasaki, T.; Sonoyama, M.; Demura, M. and Mitaku, S., Photochem. Photobiol., (2005), **81**, 1131.

[5] Flory, P. J., J. Chem. Phys., (1942), **10**, 51.

[6] Huggins, M. L., J. Phys. Chem., (1942), **46**, 151.

[7] Asakura, S. and Oosawa, F., J. Chem. Phys., (1954), **22**, 1255.

[8] Asakura, S. and Oosawa, F., J. Pol. Sci., (1958), **33**, 183.

[9] Vrij, A., Pure Appl. Chem., (1976), **48**, 471.

[10] Hek, H. D. and Vrij, A., J. Colloidal Interface Sci., (1979), **70**, 592.

[11] Hek, H. D. and Vrij, A., J. Colloidal Interface Sci., (1981), **84**, 409.

[12] Gast, A. P.; Hall, C. K. and Russel, W. B., J. Colloidal Interface Sci., (1983), **96**, 251.

[13] Lekkerkerker, H. N. W., Colloids and Surface, (1990), **51**, 419.

[14] Lekkerkerker, H. N. W.; Poon, W. C. K.; Pusey, P. N.; Stroobants, A. and Warren, P. B., Europhys. Lett., (1992), **20**, 559.

[15] Ilett, S. M.; Orrock, A.; Poon, W. C. K. and Pusey, P. N., Phys. Rev. E, (1995), **51**, 1344.

[16] Dijkstra, M.; Frenkel, D. and Hansen, J. P., J. Chem. Phys., (1994), **101**, 3179.

[17] Dijkstra, M. and Frenkel, D., Phys. Rev. Lett., (1994), **72**, 298.

[18] Dijkstra, M.; van Roij, R. and Evans, R., Phys. Rev. Lett., (1998), **81**, 2268.

[19] Dijkstra, M.; van Roij, R. and Evans, R., Phys. Rev. Lett., (1999), **82**, 117.

[20] Dijkstra, M.; van Roij, R. and Evans, R., Phys. Rev. E, (1999), **59**, 5744.

[21] Dijkstra, M.; Brader, J. M. and Evans, R., J. Phys.: Condens. Matter, (1999), **11**, 10079.

[22] Alder, B. J. and Wainwright, T. E., Phys. Rev., (1962), **127**, 359.

[23] Reiss, H.; Frisch, H. L. and Lebowitz, J. L., J. Chem. Phys., (1959), **31**, 369.

[24] Lekkerkerker, H. N. W. and Tuinier, R., Springer, New York, (2011).

[25] Buehler, R. J.; Jr., R. H. W.; Hirschfelder, J. O. and Curtiss, C. F., J. Chem. Phys, (1951), **19**, 61.

[26] Hoover, W. G. and Ree, F. H., J. Chem. Phys, (1968), **49**, 3609.

[27] Chandler, D.; Weeks, J. D. and Andersen, H. C., Science, (1983), **220**, 787.

[28] Chandler, D. and Weeks, J. D., Phys. Rev. lett., (1970), **25**, 149.

[29] Weeks, J. D.; Chandler, D. and Andersen, H. C., J. Chem. Phys., (1971), **54**, 5237.

[30] Alberts, B.; Johnson, A.; Lewis, J.; Morgan, D.; Raff, M.; Roberts, K. and Walter, P., Garland Science, New York, (2015).

[31] Alder, B. J. and Wainwright, T. E., J. Chem. Phys., (1957), **27**, 1208.

[32] Alder, B. J.; Hoover, W. G. and Young, D. A., J. Chem. Phys., (1968), **49**, 3688.

[33] Kosterlitz, J. M. and Thouless, D. J., J. Phys. C, (1973), **6**, 1181.

[34] Halperin, B. I. and Nelson, D. R., Phys. Rev. Lett., (1978), **41**, 121.

[35] Young, A. P., Phys. Rev. B, (1979), **19**, 1855.

[36] Russo, J. and Wilding, N. B., Phys. Rev. Lett., (2017), **119**, 115702.

[37] Bernard, E. P. and Krauth, W., Phys. Rev. Lett., (2011), **107**, 155704.

[38] Engel, M.; Anderson, J. A.; Glotzer, S. C.; Isobe, M.; Bernard, E. P. and Krauth, W., Phys. Rev. E, (2013), **87**, 042134.

[39] Mermin, N. D. and Wagner, H., Phys. Rev. Lett., (1966), **17**, 1133.

[40] Mermin, N. D., Phys. Rev., (1968), **176**, 250.

[41] Krebs, M. P. and Isenbarger, T. A., Biochim. Biophys. Acta, (2000), **1460**, 15.

[42] Yamashita, H.; Voìtchovsky, K.; Uchihashi, T.; Contera, S. A.; Ryan, J. F. and Ando, T., Journal of Structural Biology, (2009), **167**, 153.

[43] Krebs, M. P.; Li, W. and Halambeck, T. P., J. Mol. Biol., (1997), **267**, 172.

[44] Wang, J.; Link, S.; Heyes, C. D. and El-Sayed, M. A., Biophysical journal, (2002), **83**, 1557.

[45] Isenbarger, T. A. and Krebs, M. P., Biochemistry, (1999), **38**, 9023.

[46] Suda, K.; Suematsu, A. and Akiyama, R., J. Chem. Phys., (2021), **154**, 204904.

[47] Fulton, A. B., Cell, (1982), **30**, 345.

[48] Goodsell, D. S., Trends Biochem. Sci., (1991), **16**, 203.

[49] Minton, A. P., Curr. Opin. Biotechnol., (1997), **8**, 65.

[50] Kinjo, A. R. and Takada, S., Phys. Rev. E, (2002), **66**, 031911.

[51] Kinjo, A. R. and Takada, S., Phys. Rev. E, (2002), **66**, 051902.

[52] Ellis, R. J. and Minton, A. P., Nature, (2003), **425**, 27.

[53] Hall, D. and Minton, A. P., Biochim. Biophys. Acta, (2003), **1649**, 127.

[54] Akiyama, R.; Karino, Y.; Hagiwara, Y. and Kinoshita, M., J. Phys. Soc. Japan, (2006), **75**, 064804.

[55] Lee, J. T. and Robert, M., Phys. Rev. E, (1999), **60**, 7198.

[56] Wadati, M. and Toda, M., J. Phys. Soc. Japan, (1972), **32**, 1147.

[57] Hachisu, S.; Kobayashi, Y. and Kose, A., J. Colloid Interface Sci., (1973), **42**, 342.

[58] Pusey, P. N. and van Megen, W., Nature, (1986), **320**, 340.

[59] Tuinier, R.; Smith, P. A.; Poon, W. C. K.; Egelhaaf, S. U.; Aarts, D. G. A. L.; Lekkerkerker, H. N. W. and Fleer, G. J., Europhys. Lett., (2008), **82**, 68002.

[60] Widom, B., Science, (1967), **157**, 375.

[61] Longuet-Higgins, H. C. and Widom, B., Mol. Phys., (1964), **8**, 549.

[62] Rakovich, A.; Sukhanova, A.; Bouchonville, N.; Lukashev, E.; Oleinikov, V.; Artemyev, M.; Lesnyak, V.; Gaponik, N.; Molinari, M.; Troyon, M.; Rakovich, Y. P.; Donegan, J. F. and Nabiev, I., Nano Lett., (2010), **10**, 2640.

[63] Henderson, D., Mol. Phys., (1975), **30**, 971.

[64] Helfand, E.; Frisch, H. L. and Lebowitz, J. L., J. Chem. Phys., (1961), **34**, 1037.

[65] Salsburg, Z. W. and Wood, W. W., J. Chem. Phys., (1962), **37**, 798.

[66] Neugebauer, D. C.; Zingsheim, H. P. and Oesterhelt, D., Meth. Enzymol., (1983), **97**, 218.

[67] Thorneywork, A. L.; Abbott, J. L.; Aarts, D. G. A. L. and Dullens, R. P. A., Phys. Rev. Lett., (2017), **118**, 158001.

[68] Lin, S.-C. and Oettel, M., Phys. Rev. E, (2018), **98**, 012608.

[69] García, Á. G.; Opdam, J.; Tuinier, R. and Vis, M., Chem. Phys. Lett., (2018), **709**, 16.

[70] Suematsu, A.; Yoshimori, A. and Akiyama, R., Europhys. Lett., (2016), **116**, 38004.

[71] Velasco, E.; Navascués, G. and Mederos, L., Phys. Rev. E, (1999), **60**, 3158.

[72] Tamura, Y.; Yoshimori, A.; Suematsu, A. and Akiyama, R., Europhys. Lett, (2020), **129**, 66001.

[73] Luecke, H.; Schobert, B.; Richter, H. T.; Cartailler, J. P. and Lanyi, J. K., J. Mol Biol., (1999), **291**, 899.

[74] Sternberg, B.; L'Hostis, C.; Whiteway, C. A. and Watts, A., B. B. A–Biomembranes, 1992, **1108**, pp. 21.